Droplets and Sprays IV
Wednesday, 22 March
9:15 – 10:55

13th U. S. National Combustion Meeting
Organized by the Central States Section of the Combustion Institute
March 19–22, 2022
College Station, Texas

Statistics of the Interactions between an Underexpanded Shock Train and a Liquid Spray

Christopher B. Reuter[*]*, Steven G. Tuttle*

U.S. Naval Research Laboratory, Chemistry Division,
4555 Overlook Avenue SW, Washington, DC 20375
[*]*Corresponding Author Email: christopher.reuter@nrl.navy.mil*

Abstract: The interactions between droplets and shock waves have many applications, but few studies have investigated how the distributions of droplet diameters and droplet velocities are modified after passing through a shock. This study examines the droplet statistics upstream and downstream of shock features in an underexpanded jet by performing phase Doppler interferometry in combination with Schlieren imaging. A mixture of water and propylene glycol is employed as the liquid. It is found that passing through an oblique shock causes the droplets to break up and then agglomerate while the droplet velocity remains relatively unaffected. The measured joint probability distributions of droplet velocity and diameter for the oblique shock case indicate that the smaller droplets have higher velocities and that the larger droplets have lower velocities. On the other hand, the droplet velocities are found to decrease rapidly when passing through a normal shock in the form of a Mach disk, but the droplet diameters are not immediately affected. The velocity distributions for the Mach disk cases are found to depend on the pressure—the moderate pressure case exhibits strong bimodal behavior, but the higher pressure cases do not. The droplet statistics presented here can be used to improve computational modeling of spray-shock interactions.
Keywords: Shock wave, multiphase supersonic flow, droplet-shock interactions, phase Doppler interferometry

1. Introduction

Droplet-shock interactions occur in a variety of scenarios, including in both the ducts and across the fuel injectors of high-speed combustors. As liquid water flows into inlets or liquid fuel is injected into the cross-streams of combustor ducts, the spray evolves as it passes through oblique and normal shocks. In particular, the sudden decrease in gas velocity can cause rapid secondary droplet atomization. Although shock-driven secondary breakup has been examined in a number of studies, the majority of previous investigations have involved the interactions between shock waves and a single (often very large) droplet [1-4] or a stream of droplets [5-8].

In general, shock-spray interactions are difficult to reproduce in laboratory conditions. A supersonic wind tunnel or jet requires large flow rates of high-pressure air and the extensive infrastructure to support it. For small-scale spray jet experiments, one of the challenges is optically resolving the experimental details via methods such as phase Doppler interferometry while managing significant cold spray or heat release. Many studies in the literature have focused on only the evolution of the droplet Sauter mean diameter, D_{32}, [9] or the mean droplet velocity [10] as the spray crossed the shock wave. Menon and Gurunadhan [11] measured probability

distributions of droplet diameters within a shock train but did not have optical access to the initial shock wave, which remained inside their overexpanded nozzle for all of their conditions. Therefore, it remains difficult to understand the relationship between the droplet diameter and droplet velocity probability distributions before and after a shock wave.

To address this, the current investigation characterizes the droplet diameter and velocity statistics upstream and downstream of shock features in an underexpanded jet. Specifically, Schlieren imaging and phase Doppler interferometry measurements are performed along the centerline of the two-phase flow issuing from an open-pipe atomizer. This study is part of a broader investigation to characterize droplet-shock interaction in compressible flows and to develop statistical and numerical tools for modeling the associated behaviors.

2. Experiment

A. Liquid Spray System

The experimental platform consists of an underexpanded jet in the form of a 178-mm long tube with an inner diameter of 3.18 mm at the exit. As seen in Figure 1, a series of decreasing diameter brazed tubes (with a final inner diameter of 0.51 mm) deliver the liquid to the center of the air flow 175 mm upstream of the exit. Thus, the system is essentially an open-pipe atomizer. Pressure ports near the jet entrance and exit provide static pressure measurement sites. The liquid is composed of a 50%-50% mixture of water and propylene glycol (propane-1,2-diol or PG) by volume. This mixture, with a freezing point of approximately 240 K, remains liquid even as the high velocity depresses the static temperature of the air and also maintains a low enough viscosity for the pump to drive the liquid. The PG/water mixture has a density of 1034 kg/m^3, a viscosity of 5.6 mPa-s, and a refractive index of 1.388 at room temperature (298 K).

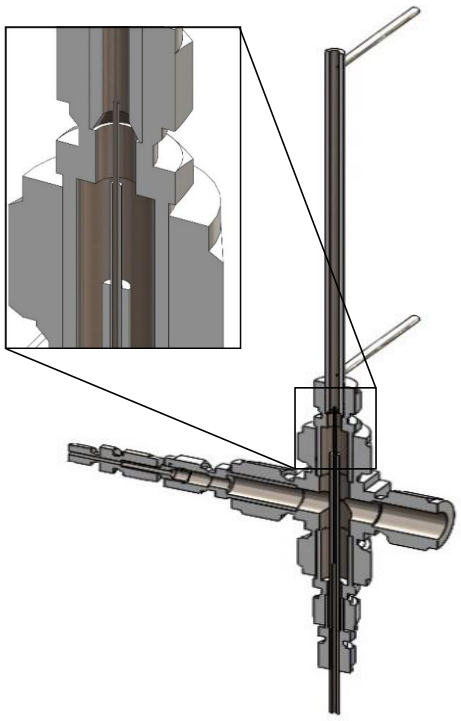

Figure 1: Cross-sectional view of the atomizer. Air is injected into the right side, liquid is injected at the bottom, and a thermocouple port is located on the left side. Note that the atomizer is placed downward in the experiment.

Air and liquid flow is controlled and recorded via a PC-operated data acquisition system. The air flow is metered by an Alicat pressure controller (PCD-3000PSIG-D-DB9M-PCA13/10P) which is supplied from a dome loaded valve (SwageLok RDN2-02-VVK) that directs air to a 1.11 mm-diameter and metering tube (Flow Systems) rated to an upstream pressure of 20.6 MPa. A Bronkhorst Coriolis flow meter controls the liquid flow from a pressurized manifold. A pump continuously cycles the liquid into the pressurized manifold and then back into a catch reservoir that also catches the spray droplets. The manifold system is composed of a motor-powered, high-pressure plunger pump, which pumps the liquid into the manifold with the assistance of a Blacoh high pressure dampener on a branch. A hydraulic back pressure regulator allows for control of the manifold back pressure before the flow returns to the reservoir. Overall, the experimental platform provides the advantage of studying shock-spray interactions outside of a complex and expensive supersonic wind tunnel.

Experimental conditions of the gas flow are listed in Table 1. Given the underexpanded conditions of the jet, it can be assumed that the flow is at the speed of sound at the nozzle exit. $P_{t,f,set}$ is the pressure specified to the pressure controller, while $P_{t,f,read}$ is that which is measured at the pressure controller. $P_{t,v,u}$ is the total pressure upstream of the venturi, $T_{t,v,u}$ is the total temperature upstream of the venturi, $P_{t,v,d}$ is the pressure downstream of the venture, and $\dot{m}_v$ is the calculated mass flow through the venturi. $P_{s,n}$ is the static pressure near the nozzle exit.

Table 1: Flow conditions examined during this study.

$P_{t,f,set}$ ($\times 10^6$ Pa)	$P_{t,f,read}$ ($\times 10^6$ Pa)	$P_{t,v,u}$ ($\times 10^6$ Pa)	$T_{t,v,u}$ (K)	$P_{t,v,d}$ ($\times 10^5$ Pa)	$\dot{m}_v$ (g/s)	$P_{s,n}$ ($\times 10^5$ Pa)
3.00	3.00	2.84	281	4.76	6.49	2.12
4.00	4.00	3.83	275	6.28	8.85	2.85
5.00	5.00	4.85	275	7.44	11.2	3.41
6.00	6.00	5.86	278	8.74	13.5	4.03

B. Optical Diagnostics

Schlieren imaging of the shock structures is first performed to establish the location and nature of the shock structures in the flow. A quartz tungsten-halogen lamp (Thorlabs QTH10) provides the light, which passes through a collimating aspheric condenser lens and an aperture and then is directed by a spherical mirror through the supersonic jet. Another spherical lens directs the light through a #2 neutral density filter and into a camera (Mightex) with an exposure time of 0.4 ms.

Spray measurements of the droplet diameters and velocities are performed with an Artium phase Doppler interferometry system (2D PDI-200). A 532 nm laser is used to measure the vertical velocity and droplet diameter while a 561 nm laser is used to measure the horizontal velocity. Both the transmitter and receiver use 350 mm focal lengths. The transmitting beam separation is 25 mm. This provides a velocity range of -200 to 800 m/s and a droplet range of 0.5-100 μm. Data collection rates are typically in the range of 1-10 kHz in numbers of around 10,000 samples.

3. Results and Discussion

Single-phase Schlieren images, shown in Figure 2, reveal the shock wave structures as the pressure increases from 3 MPa to 6 MPa. As the set pressure and corresponding mass flow increases, the primary oblique shock turns into a small normal shock at the center of the jet; the normal shock increases across the width of the jet and moves further downstream as the supply pressure and mass flow increase. The structures in Figure 2 are typical for underexpanded supersonic jet flows, with the 3 MPa case being a classic "moderately underexpanded jet" with shock diamonds and the 4 MPa, 5 MPa, and 6 MPa cases falling into the category of "highly underexpanded jets" with Mach disks [12].

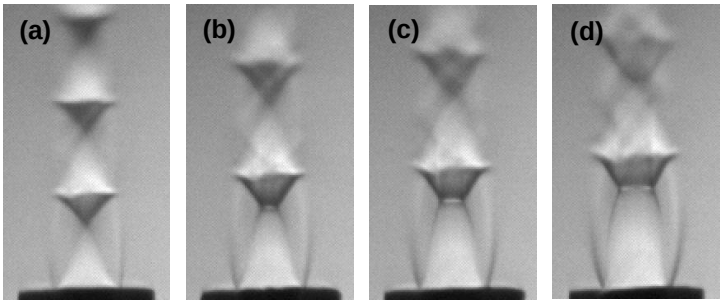

Figure 2: Schlieren images of the air jet (no liquid injection) with increasing supply pressure.

When liquid is injected at 5 mL/min (0.087 g/s) for the 3 MPa case, streaks near the nozzle exit can be seen in Figure 3a, which results from the liquid film at the outer edge of the flow being sheared and atomized. The location of the oblique shock also shifts very slightly downstream. Figure 3b shows the centerline profiles of droplet velocity and diameters at the same condition as the Schlieren image. The black dashed lines indicate the approximate locations where the oblique shocks converge and where the start of an expansion wave occurs [13]. There is a monotonic increase in the mean droplet velocity (U_{mean}) all the way to the oblique shock at ~3.1 mm. Afterwards, the velocity dips and then levels off. It is unclear how much the gas velocity increases through the expansion wave, but it is clear that the droplet velocities do not change significantly.

There are more pronounced variations in droplet diameters than droplet velocities for oblique shocks, which agrees with the results of Menon and Gurunadhan for water droplets [11]. The arithmetic mean diameter, D_{10}, holds steady as the spray exits the nozzle, increases slightly before the oblique shock, and then decreases in the ~0.3 mm following the oblique shock. However, D_{10} then quickly rises to its highest value before decreasing again following the expansion wave. D_{32}, the Sauter mean diameter, displays more scatter than D_{10} and notably decreases before the oblique shock even though D_{10} is relatively constant or even slightly rising. The differences between the behaviors of D_{32} and D_{10} can be best understood by examining the droplet probability distributions.

Figure 4a shows the measured droplet diameter distributions along the centerline for the 3 MPa, 5 mL/min case, with the black dashed lines again indicating the locations of the oblique shock and expansion wave from the Schlieren image. Details of the distribution are evident which D_{10} and

D_{32} alone are unable to reveal. The most probable diameter is near 8 µm for almost all of the spray but varies significantly in probability from ~0.17 near the oblique shock to ~0.085 near the expansion wave. The largest diameters with non-negligible probability are near 30 µm initially, decrease to ~26 µm after the oblique shock, and then rapidly rise to ~55 µm before falling again after the expansion wave.

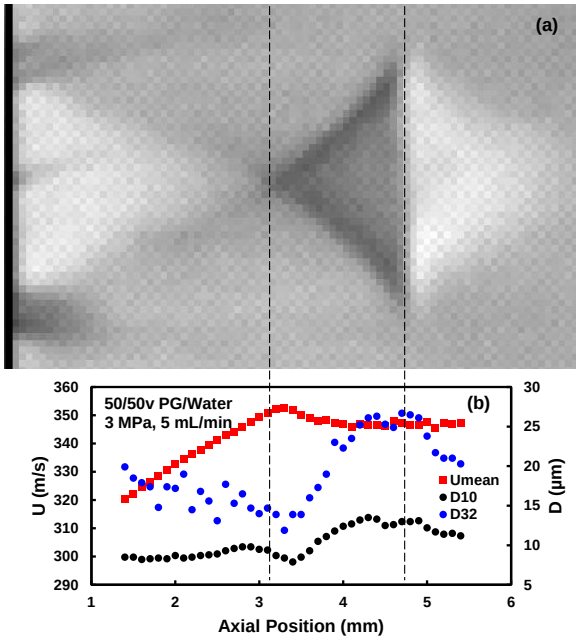

Figure 3: (a) Schlieren image and (b) centerline profiles of U_{mean}, D_{10}, and D_{32} for the 3 MPa, 5 mL/min case. The black dashed lines indicate the locations of the shock and expansion waves.

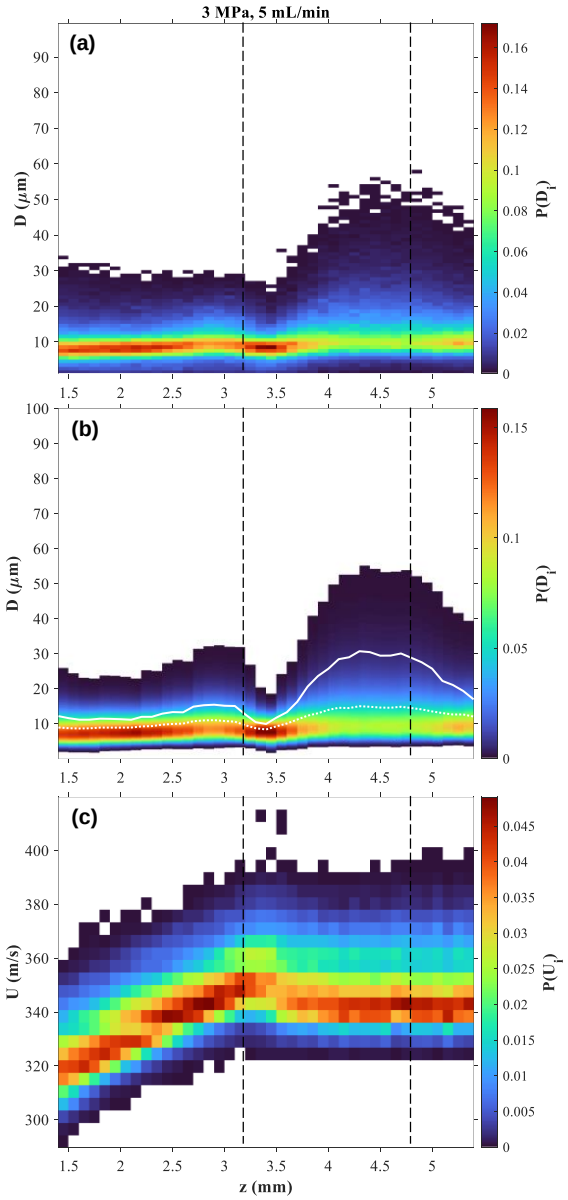

Figure 4: Centerline profiles of (a) droplet diameter distributions, (b) probability distribution fits to droplet diameters, and (c) droplet velocity distributions for the 3 MPa, 5 mL/min case. The white dotted lines and white solid lines in (b) indicate the fitted D_{10} and D_{32}, respectively.

The probability distribution fits (PDFs) to the droplet diameter measurements are shown in Figure 4b. An exponentiated Weibull distribution [14], with a typical R^2-value of 0.95 or higher, fits the measurements slightly better than a log-normal distribution. The D_{32} derived from the fit is much smoother than the measured D_{32}, for which a few large (>70 μm) droplets can exert a disproportionate influence. The fitted D_{32} now follows the same trend as D_{10}—fairly steady at the beginning, a slight increase before the oblique shock, a sharp decrease and then rapid increase after the oblique shock, and another decrease following the expansion wave. The measured droplet velocity distributions are also shown in Figure 4c but are much less dramatic for the 3 MPa case than the other cases at higher pressures with normal shocks.

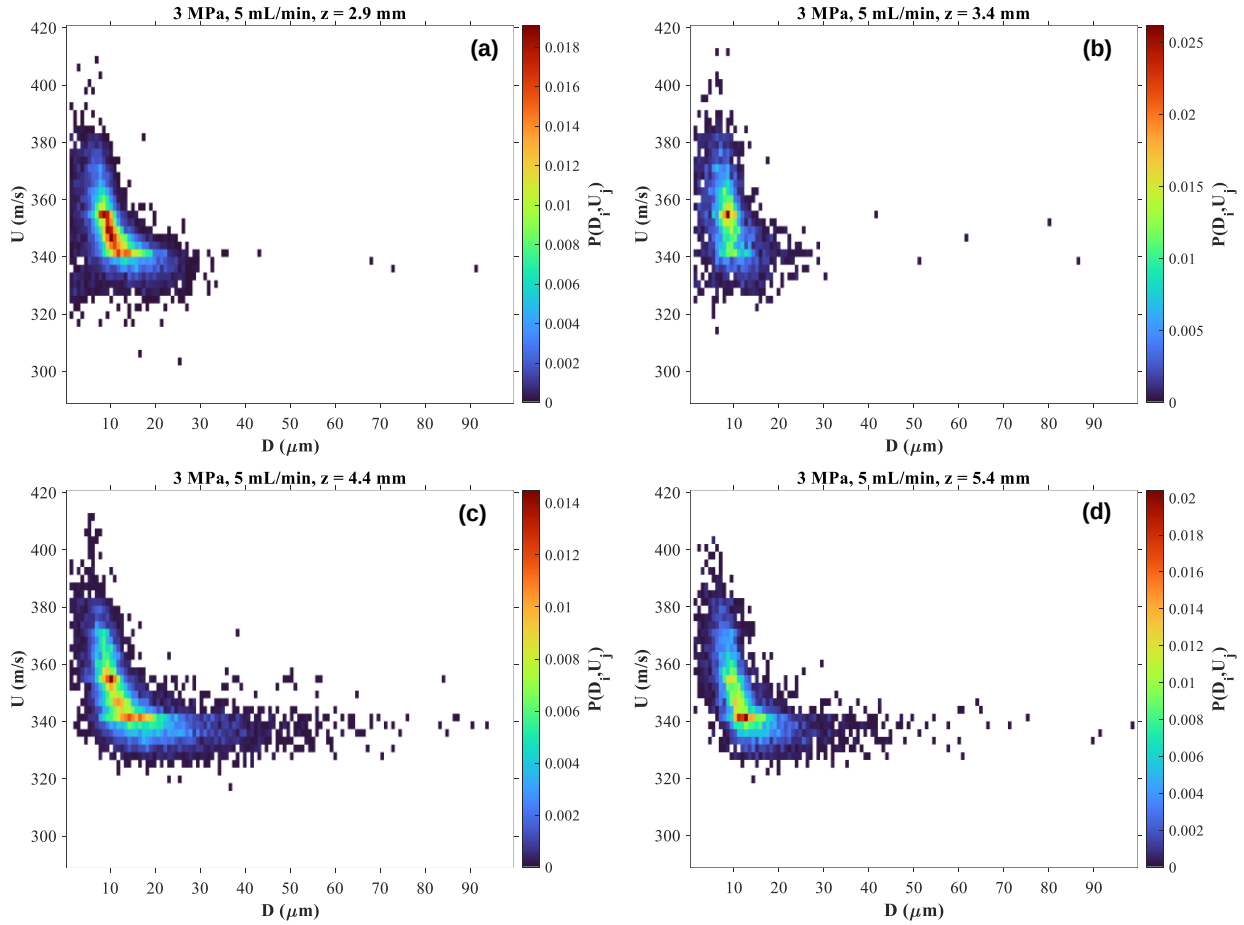

Figure 5: Joint probability distributions of droplet velocity and diameter for the 3 MPa, 5 mL/min case at axial locations of (a) 2.9 mm, (b) 3.4 mm, (c) 4.4 mm, and (d) 5.4 mm.

Figure 5 shows the measured joint probability distributions (JPD) at several different axial locations. Prior to the oblique shock at 2.9 mm (Figure 5a), the JPD displays negative covariance in that the larger droplets tend to have lower velocities. After the oblique shock and near the minimum value of D_{10}, small droplets dominate the JPD, and there is much less correlation between the droplet diameter and the droplet velocity. As the spray approaches the expansion wave (Figure 5c), the JPD expands to cover much larger droplets at low velocities. Finally, past the expansion wave in Figure 5d, the JPD returns to a similar profile as in Figure 5a, with the most

probably velocity being slightly lower. Therefore, it appears that the oblique shock structures of the "moderately underexpanded jet" can have dramatic effects on the distribution of the droplet diameters (with alternating breakup and agglomeration) but far fewer impacts on the droplet velocity.

The impact of a Mach disk on the centerline droplet statistics is shown in Figure 6. U_{mean} increases monotonically before the normal shock, drops immediately post-shock, and then levels off after passing through the expansion wave. D_{10} is relatively constant as far as 0.5 mm beyond the Mach disk before rising to its peak ~1 mm post-shock. D_{10} then decreases slightly from its peak value and remains more or less unchanged as it passes through the expansion wave. The measured D_{32} is again more scattered but follows most of the same trends as D_{10}. It remains between 13 and 18 µm through the Mach disk and then sharply increases to a peak value of 34 µm about 1 mm after the shock. D_{32} then slowly decreases as the droplets move though the expansion wave.

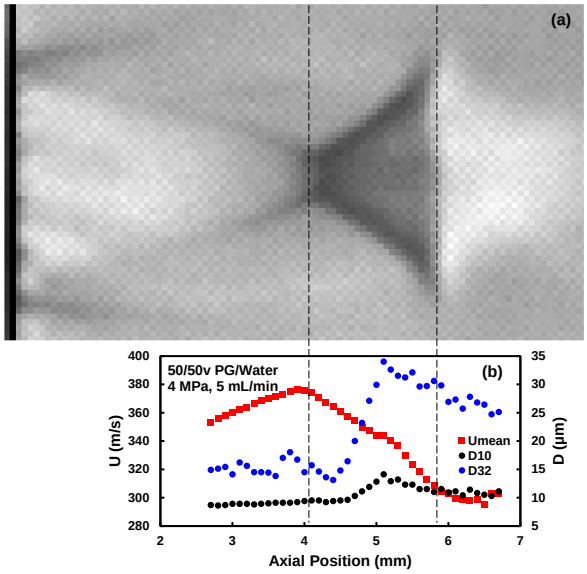

Figure 6: (a) Schlieren image and (b) centerline profiles of U_{mean}, D_{10}, and D_{32} for the 4 MPa, 5 mL/min case.

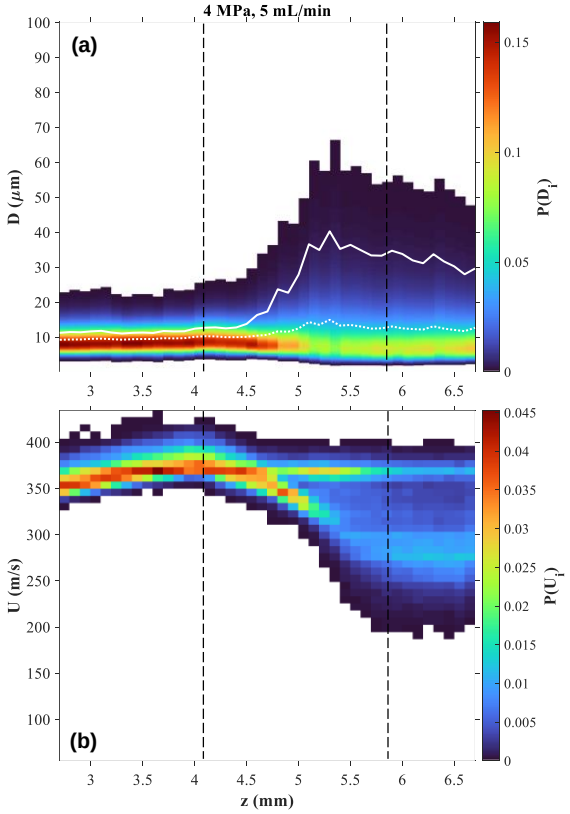

Figure 7: Centerline profiles of (a) probability distribution fits to droplet diameters and (b) droplet velocity distributions for the 4 MPa, 5 mL/min case.

Figure 7 shows the fitted droplet diameter and measured droplet velocity distributions for the 4 MPa, 5 mL/min case. The fitted diameter PDFs are quite consistent until ~0.5 mm after the shock, after which an interesting phenomena occurs. The largest diameters increase rapidly and, consequently, D_{32} increases as well. However, the most probable diameter actually decreases; as

a result, D_{10} rises from 10 µm at the Mach disk to 13 µm at the expansion wave at the same time as D_{32} increases from 13 µm to 32 µm. Additionally, the centerline droplet velocity probability distributions in Figure 7b reveal remarkable trends that cannot be gathered from U_{mean} alone. Upon passing through the Mach disk, the droplet velocity distribution becomes bimodal, with an upper branch of high probability around 370 m/s and a lower branch that consistently decreases until it reaches the expansion wave. After the expansion wave, the lower branch is steady near 275 m/s.

The JPD of droplet velocity and diameter for the 4 MPa case is shown in Figure 8. Shortly after passing through the Mach disk, small droplets with very low velocities (<150 m/s) appear in Figure 8a. Continuing downstream, the JPD expands in both directions and begins to display bimodal behavior, with one "island" of larger droplets at larger velocities and another "island" of smaller droplets at smaller velocities. It is expected that the pocket of smaller droplets is more representative of the gas-phase velocity and that the pocket of larger droplets (with larger Stokes numbers) cannot follow the flow as easily.

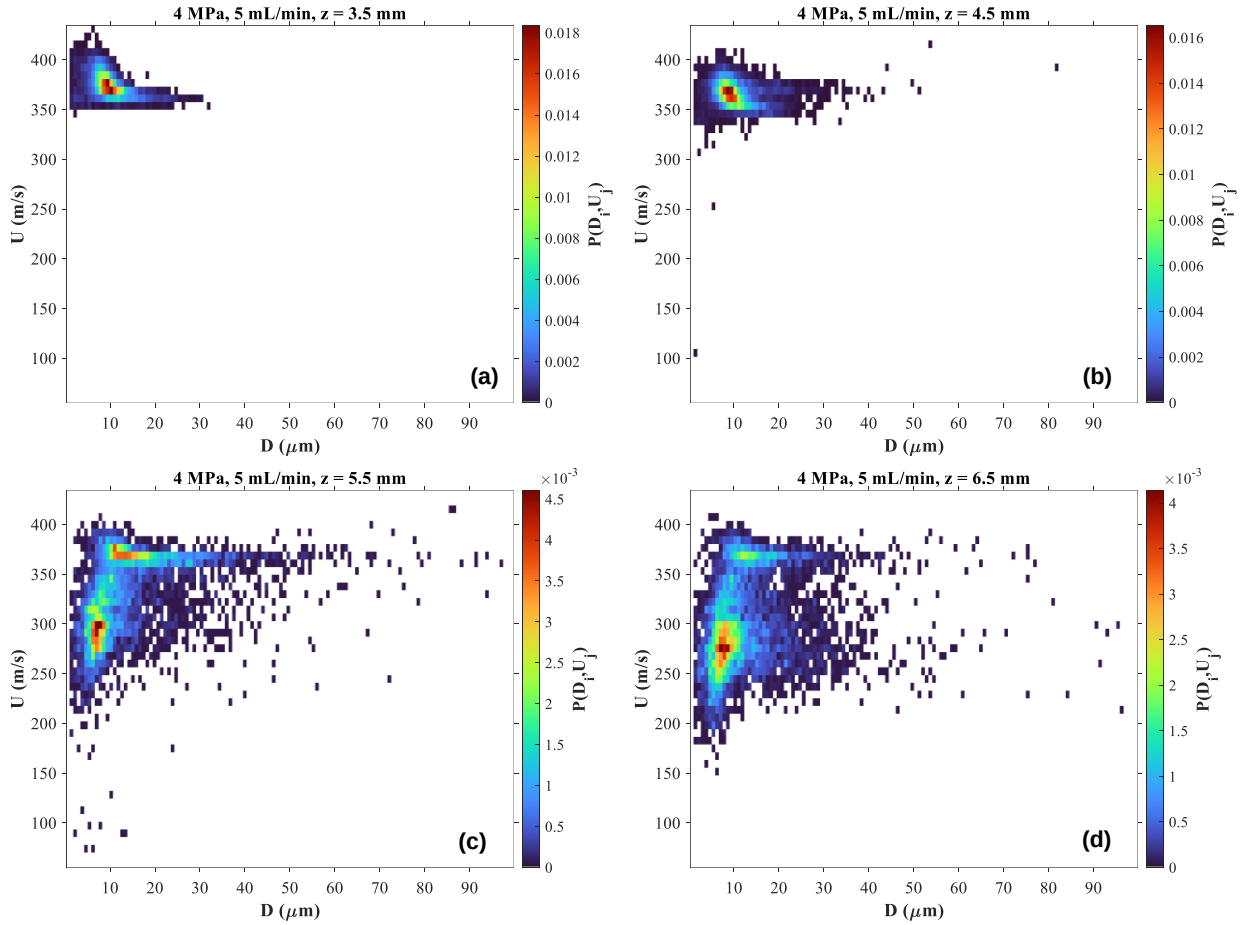

Figure 8: Joint probability distributions of droplet velocity and diameter for the 4 MPa, 5 mL/min case at axial locations of (a) 3.5 mm, (b) 4.5 mm, (c) 5.5 mm, and (d) 6.5 mm.

Figures 9 and 10 show the centerline droplet diameter and velocity statistics for the 5 MPa and 6 MPa cases with 5 mL/min of liquid injection. In contrast to the 4 MPa case, the fitted droplet diameter PDFs of the 5 MPa and 6 MPa cases are fairly similar to one another in that the droplet

diameters seem to be unaffected by the Mach disk and increase shortly after the expansion wave. Sommerfeld and Kurian [11] also observed that the droplet diameters did not considerably change as their water droplets passed through a Mach disk, which they surmised was due to the gas velocity and the droplet velocity being nearly equal post-shock. However, they measured U_{mean} values of no larger than 230 m/s near the shock, but in this study U_{mean} is approximately 385 m/s in the vicinity of the shock. Therefore, it does not seem that their explanation holds for this study with almost all of the droplets remaining above 330 m/s (equivalent to Mach 1 for the gas phase) after the normal shock.

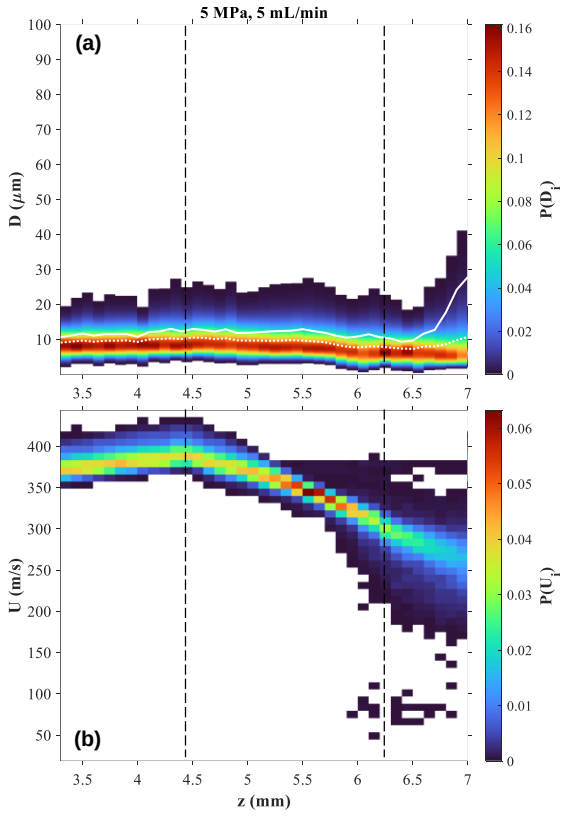

Figure 9: Centerline profiles of (a) probability distribution fits to droplet diameters and (b) droplet velocity distributions for the 5 MPa, 5 mL/min case.

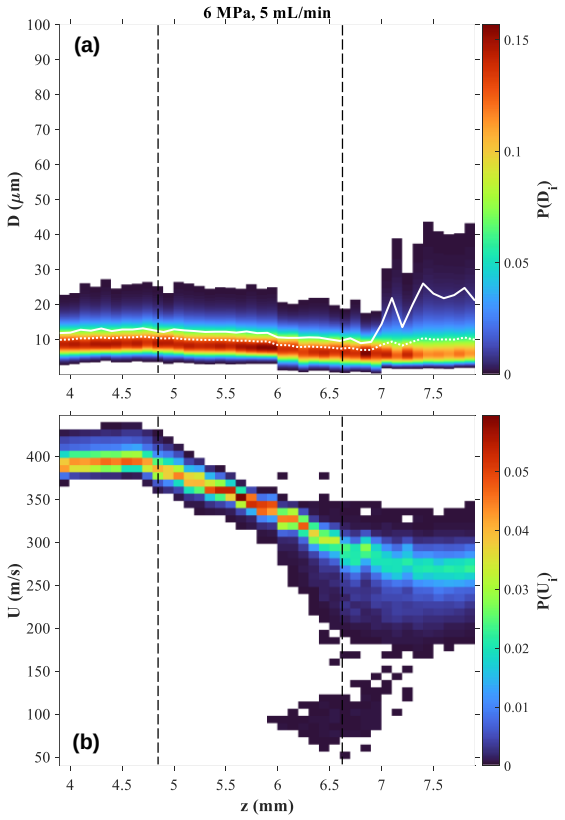

Figure 10: Centerline profiles of (a) probability distribution fits to droplet diameters and (b) droplet velocity distributions for the 6 MPa, 5 mL/min case.

The velocity probability distributions for the 5 MPa and 6 MPa cases do not have an upper branch near 370 m/s as the 4 MPa case does. Rather, the most probable velocity decreases monotonically between the Mach disk and the expansion wave. An isolated region of very low velocity (<150 m/s) is also present, although it has low probability. Additionally, as can be expected from their droplet velocity distributions, the JPDs for the 5 MPa and 6 MPa cases (not shown) display less bimodal behavior compared to the 4 MPa case. Specifically, the upper "island" is not present, which can be deduced from the droplet velocity distributions in Figures 9b and 10b.

4. Conclusions

Phase Doppler interferometry was used to measure the droplet statistics along the centerline of an underexpanded jet with liquid water/propylene glycol injection. When combined with Schlieren imaging, the measurements revealed that the case with oblique shocks and the three cases with normal shocks in the form of Mach disks behaved quite differently. The droplet diameters decreased and then increased when the spray passed through an oblique shock but were less affected by the normal shocks. On the other hand, the droplet velocities remained steady after the oblique shock but decreased consistently after the normal shocks. The joint probability distributions of the droplet velocity and diameter also revealed opposing trends. The oblique shock case tended to have the largest droplets moving at the slowest velocities, but the normal shock cases had the smallest droplets moving at the slowest velocities. Future plans for this work include computations of the gas-phase velocity and gas-phase density for an accurate estimation of the Weber number, which governs droplet breakup.

5. Acknowledgements

This research is supported by the Office of Naval Research under the Naval Research Laboratory Base Program.

6. References

[1] B.E. Gel'fand, S.A. Gubin, S.M. Kogarko, Various forms of drop fractionation in shock waves and their special characteristics, J. Eng. Phys. 27 (1974) 877-882.
[2] L.-P. Hsiang, G.M. Faeth, Drop deformation and breakup due to shock wave and steady disturbances, Int. J. Multiphase Flow 21 (1995) 545-560.
[3] T.G. Theofanous, Aerobreakup of Newtonian and viscoelastic liquids, Annu. Rev. Fluid Mech. 43 (2011) 661-690.
[4] S. Sharma, A.P. Singh, S.S. Rao, A. Kumar, S. Basu, Shock induced aerobreakup of a droplet, J. Fluid Mech. 929 (2021) A27.
[5] A.R. Hanson, E.G. Domich, H.S. Adams, Shock tube investigation of the breakup of drops by air blasts, Phys. Fluids 6 (1963) 1070-1080.
[6] A.A. Ranger, J.A. Nicholls, Aerodynamic shattering of liquid drops, AIAA J. 7 (1969) 285-290.
[7] H. Hirahara, M. Kawahashi, Experimental investigation of viscous effects upon a breakup of droplets in high-speed air flow, Exp. Fluids 13 (1992) 423-428.
[8] Y. Kim, J.C. Hermanson, Breakup and vaporization of droplets under locally supersonic conditions, Phys. Fluids 24 (2012) 076102.
[9] K. Issac, A. Missoum, J. Drallmeier, A. Johnston, Atomization experiments in a coaxial coflowing Mach 1.5 flow, AIAA J. 32 (1994) 1640-1646.
[10] M. Sommerfeld, J. Kurian, Droplet behaviour in underexpanded supersonic jets, Shock Waves@ Marseille III, Springer (1995), pp. 95-100.
[11] S. Menon, M. Gurunadhan, Droplet behavior in overexpanded supersonic two-phase jets, Int. J. Multiphase Flow 152 (2022) 104076.
[12] E. Franquet, V. Perrier, S. Gibout, P. Bruel, Free underexpanded jets in a quiescent medium: A review, Prog. Aerosp. Sci. 77 (2015) 25-53.
[13] B. André, T. Castelain, C. Bailly, Experimental exploration of underexpanded supersonic jets, Shock Waves 24 (2014) 21-32.
[14] G.S. Mudholkar, D.K. Srivastava, Exponentiated Weibull family for analyzing bathtub failure-rate data, IEEE Trans. Reliab. 42 (1993) 299-302.

13th U.S. National Combustion Meeting
Organized by the Central States Section of the Combustion Institute
March 19–22, 2023
College Station, Texas

Modeling Droplet Vaporization with Multicomponent Diffusion and Combustion Properties with Accuracy, Efficiency, and Flexibility

Simcha Singer[1,*]

[1]*Department of Mechanical Engineering, Marquette University, Milwaukee, WI 53233, USA*
[*]*Corresponding Author Email: simcha.singer@marquette.edu*

Abstract: Droplet vaporization submodels for spray combustion CFD codes require accuracy, efficiency, and the flexibility to deal with changing environments. Diffusion of vaporized (and condensable) species in the film surrounding the droplet are most accurately represented using the multicomponent Maxwell-Stefan equations, especially for the high-pressure, near-critical conditions characteristic of modern jet and diesel engines. However, the Maxwell-Stefan formulation leads to high computational costs, especially for large discrete physical-chemical surrogates, which are needed to emulate a real multicomponent fuel's vaporization behavior and physical properties, in addition to its chemical behavior (combustion property targets, or CPTs). Physical–chemical surrogates have also been shown to have difficulty in emulating the instantaneous, distillation-resolved CPTs, which vary throughout droplet vaporization. An alternative "hybrid" framework solves this problem by combining an efficient and flexible continuous thermodynamic model (CTM) for droplet vaporization with an adaptive chemical surrogate formulated using functional group matching to the instantaneous vaporization flux from the droplet. The CTM of the hybrid approach is modified here to model droplet vaporization using a continuous version of the Maxwell-Stefan equations in the film surrounding the droplet. The computational efficiency of the CTM makes the implementation of the Maxwell-Stefan framework feasible, and functional group fluxes and instantaneous CPTs are more accurately predicted by the hybrid approach than the physical-chemical surrogate method for the moderate-pressure conditions tested.

Keywords: *Preferential vaporization; surrogates; continuous thermodynamic model; functional groups.*

1. Introduction

Gasoline, jet fuels, and diesel fuel contain hundreds to thousands of hydrocarbons from several chemical families [1]. To achieve computational tractability, computational fluid dynamics (CFD) simulations for spray combustion employ smaller surrogate mixtures to represent the behavior of multicomponent fuels. "Chemical surrogates" composed of just a few species are formulated to match certain combustion property targets (CPTs) of the full multicomponent liquid fuel (the target fuel) when it is present in the same composition in the gas-phase (i.e., the fully *pre-vaporized* fuel). However, small chemical surrogates are not formulated to replicate the fuel's vaporization behavior and cannot represent the phenomena of preferential vaporization, in which species vaporize from the droplets at different rates. It has been experimentally demonstrated that preferential vaporization can influence device-scale combustion behavior, like lean blowout [2] and flashback [3].

The standard approach to capturing the impact of preferential vaporization involves the use of "physical-chemical surrogates" which are formulated to emulate the target fuel's distillation curve, in addition to its pre-vaporized CPTs [4–6]. However, the physical-chemical surrogate approach has drawbacks associated with accuracy, computational efficiency, and flexibility when incorporated in CFD codes for spray combustion. First, although the physical-chemical surrogate mimics the target fuel's distillation curve *in addition to* its pre-vaporized CPTs, nothing guarantees that the *instantaneous CPTs of the vaporizing flux* will match those of the target fuel throughout vaporization, as noted in [7] and demonstrated in [8]. Thus, the instantaneous source terms supplied by the droplet model to the Eulerian phase of a spray combustion simulation may not accurately represent the chemical properties of the real vaporizing fuel at that location and time. Second, since a significantly larger surrogate is required to emulate the target fuel's distillation curve in addition to its CPTs, the computational efficiency of the CFD code will be reduced, as more fuel species must now be tracked in the Eulerian phase following vaporization. Third, it is not obvious how physical-chemical surrogates used for the liquid fuel droplets can account for the presence of Eulerian phase species other than those comprising the physical-chemical surrogate. For example, due to pyrolysis chemistry, hydrocarbon species beyond those in the surrogate may surround the droplets, and even condense from the vapor phase. This may limit the flexibility of the physical-chemical surrogate approach.

To capture the impact of preferential vaporization with accuracy, efficiency, and flexibility, a new approach for modeling droplet vaporization together with adaptive chemical surrogate formulation has been developed [8,9]. Multicomponent droplet vaporization is modeled using a computationally efficient *continuous thermodynamic* modeling (CTM) framework with a quadrature-based moment method [10], rather than with discrete surrogate components. A functional group matching (FGM) procedure then takes the output of the droplet vaporization model and computes the composition of an adaptive chemical surrogate flux composed of just a few *discrete* species, to serve as the source (or sink) term for the Eulerian phase of the CFD solver. FGM ensures that the distribution of key functional groups (FGs) in the flux from the droplet matches that of the chemical surrogate, which implies that the combustion behavior will also be accurately emulated, as demonstrated by Won et al. [4]. It has been shown the hybrid method generally produces a more accurate solution for instantaneous functional group (FG) fluxes and CPTs than the physical-chemical surrogate approach. Also, whereas physical-chemical surrogates generate Eulerian-phase source terms consisting of 9-15 discrete species, the hybrid approach produces a smaller chemical surrogate source term via FGM, reducing the computational cost to the CFD solver. Third, the CTM framework employed by the hybrid method for droplet vaporization modeling can readily accommodate the presence of arbitrary species in the boundary layer surrounding the droplets. This increases the flexibility of the model compared to physical-chemical surrogate approaches and renders it applicable to a range of engine environments, including those in which condensation occurs.

In this paper, the physical model for droplet vaporization is modified to incorporate Maxwell-Stefan diffusion in the boundary layer surrounding the droplet. This is important for high-pressure and transcritical conditions characteristic of modern engines, in which the Maxwell-Stefan framework or an equivalent [11] is essential for accurate diffusion modeling. The Maxwell-Stefan diffusion equations are incorporated in the standard discrete component model (DCM) framework used by the physical-chemical surrogate approach and then in the CTM framework employed by the hybrid model. The performance of the hybrid model and the prevailing physical-chemical surrogate approach with Maxwell-Stefan diffusion submodels are then compared.

2. Droplet Vaporization Models

2.1 Physical Model for Droplet Vaporization with Maxwell-Stefan Diffusion

The previous version of the physical model [8,10] is among the class of models that assumes quasi-steady vapor-phase behavior, as discussed by Sirignano [12]. That version of the physical model employed Fick's law of diffusion with a single averaged diffusion coefficient in the vapor phase, along with the Peng-Robinson equation of state, and finite rates of mass and heat transfer within the droplet. It was validated with Runge's [13] data on JP-8 droplets and Nomura's [14] data on heptane droplets with good agreement [8] at lower pressures. To expand the droplet vaporization model's applicability to realistic engine environments in which the pressure exceeds the critical pressure of most fuel components, it is necessary to incorporate several modifications.

For multicomponent mixtures, cross-coupling diffusion effects become important near the critical region [15,16]. Therefore, simple diffusion models lacking cross-coupling effects that are typically used in droplet models may be innacurate and should be replaced with formulations based on Maxwell-Stefan models, the equivalent Generalized Fick's Law, or a suitable alternative [11]. Tonini and Cossali presented a (DCM) droplet model based on the Maxwell-Stefan relations for quasi-steady, low-pressure transport across an ideal gas film [17]. Toor [18] and Stewart and Prober's [19] linearized theory faciliates an analytical solution.

To modify the original droplet vaporization model for Maxwell-Stefan diffusion, every occurrence of the total vapor molar flux, N_{tot}, and the *n* individual species vapor molar fluxes, N_i, between the droplet and the surrounding film in the governing equations for species and energy must be replaced (and the classical Spalding transfer number, B_M, is no longer relevant). The individual species vapor molar fluxes, N_i, with units of mol/m^2/s are related to the diffusive fluxes, J_i, and the mole fractions, x_i, via

$$N_i = J_i + x_i N_{Tot} \tag{1}$$

In the Maxwell-Stefan film theory framework, the *n-1* independent diffusive fluxes, J_i, for each species *i* are calculated from the solution of a system of coupled nonlinear ordinary differential equations, which requires matrix inversion [15] ($\vec{J}$ represents all the J_i):

$$\vec{J} = \frac{C_g}{R\left(1-R/R_f\right)}\left[\bar{\bar{D}}\right]\left[\bar{\bar{\psi}}\right]\left(\exp\left[\bar{\bar{\psi}}\right] - \left[\bar{\bar{I}}\right]\right)^{-1}\left(x_{g,s} - x_{g,\infty}\right) \tag{2}$$

The matrix $\left[\bar{\bar{D}}\right]$ is constant across the film using the linearized theory and is evaluated at an average (reference) point in terms of the Maxwell-Stefan diffusion coefficient matrix, $\left[\bar{\bar{B}}\right]$

$$\left[\bar{\bar{D}}\right] = \left[\bar{\bar{B}}\right]^{-1} \tag{3}$$

which depends on the mole fractions, x_i, and the Maxwell-Stefan diffusivities, $\widetilde{D}_{ij}$ [15]:

$$\begin{cases} B_{ii} = \frac{x_i}{\widetilde{D}_{in}} + \sum_{\substack{k=1 \\ i\neq k}}^{n} \frac{x_k}{\widetilde{D}_{ik}} \\ B_{ij} = -x_i\left(\frac{1}{\widetilde{D}_{ij}} - \frac{1}{\widetilde{D}_{in}}\right) \end{cases} \tag{4}$$

The binary Maxwell-Stefan diffusivities are evaluated here using the Fuller correlation and depend on pressure, temperature, molecular weights, and atomic diffusion volumes. The matrix $\left[\bar{\bar{\psi}}\right]$ depends on the total molar flux, N_{tot}, and is given by [15]:

$$\left[\bar{\bar{\psi}}\right] = N_{tot}\frac{R\left(1-R/R_f\right)}{C_g}\left[\bar{\bar{B}}\right] \tag{5}$$

The total molar flux is obtained from a "bootstrap condition [15]," which in the case of droplet vaporization is typically taken to be that of Stefan diffusion, in which the air surrounding the droplet has zero flux. In this case, the total molar flux is given by

$$N_{tot} = \frac{1}{x_{air}} \sum_{\substack{k=1 \\ k \neq air}}^{n} J_k \tag{6}$$

The total molar flux is now treated as a state variable, since the diffusive fluxes, J_k, depend on N_{tot}. The Spalding heat transfer number, which appears in the energy equation, and the governing equation for the evolution of droplet radius are now written explicitly in terms of N_{tot} rather than B_M. Similarly, the governing equations for the surface mole fractions are written in terms of N_i.

2.2 Target Fuel for the Full DCM

The full DCM solves equations for every species in a target fuel. For a given physical model and target fuel composition, it is an exact representation of the multicomponent nature of the process and can be used to assess the accuracy of the hybrid approach and the physical-chemical surrogate approach. The Jet-A (POSF-10325) target fuel composition used here is based on Edwards [20], in which the 67 species comprising the fuel are specified by carbon number and chemical family. The isomeric composition for the target fuel is taken to be the same as [21]. It was verified [8] that the 67 components reproduce the fuel's measured distillation curve and CPTs (derived cetane number, DCN, hydrogen to carbon ratio, H/C, and molecular weight, MW).

2.3 Hybrid Droplet Vaporization - Adaptive Chemical Surrogate Model

The original hybrid method [9] (Fig. 1, top) includes an efficient analytical delumping step to recover the mole fractions and fluxes of every discrete species in the target fuel using the results of the CTM calculation. These fluxes are input to the FGM model to calculate the instantaneous composition of the small adaptive chemical surrogate which can serve as the source term for the Eulerian phase.

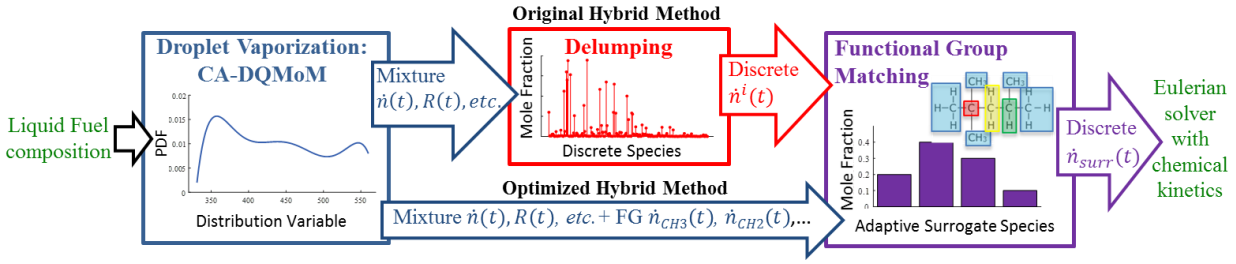

Fig. 1: Schematic of the hybrid droplet vaporization-adaptive surrogate methods. Original hybrid method with delumping and the optimized hybrid method with direct prediction of FG fluxes.

Although delumping is compatible with most quasi-steady droplet models developed for use in CFD codes, it is restricted to physical models in which all nonlinearity in the species mole fractions appears in terms associated with the *mixture*. This condition is not satisfied for certain submodels required for high-pressure and transcritical conditions, like the Maxwell-Stefan transport model outlined in Section 2.1. Therefore, an "optimized hybrid" method (Fig. 1, bottom) has been developed [8], in which the CTM can *directly* predict the FG fluxes required by the FGM in addition to the physical properties and droplet vaporization behavior.

2.3.1 CA-DQMoM for Droplet Vaporization Model

The coupled algebraic-direct quadrature method of moments (CA-DQMoM) is used to solve the differential-algebraic system of equations for multicomponent droplet vaporization [10]

using a continuous distribution *without assuming any functional form*. CA-DQMoM extends previous quadrature-based moment methods for well-mixed droplets to account for finite rates of internal transport and internal gradients of temperature and species. Quadrature-based moment methods are superior to typical CTM approaches which employ pre-determined distributions (e.g., gamma distributions) as a function of molecular weight or normal boiling temperature, since pre-determined distributions will not remain valid for liquid and vapor phases as they become distorted due to vaporization and/or condensation. In this paper, four quadrature nodes and weights are used for each distribution. Mathematical details of the CA-DQMoM droplet vaporization model are elsewhere [10]. In this paper, the model is modified to incorporate Maxwell-Stefan diffusion.

A CTM implementation of Maxwell-Stefan diffusion in a Loschmidt tube and across a steady film have recently been provided by Moraes et al. [22]. Like the CTM treatment of other equations, the Maxwell-Stefan equations are written in continuous form as a function of some distribution variable, I (see Section 2.3.2) and a moment transform is then applied. Using CA-DQMoM, a Gaussian quadrature is then employed to write the moment-transformed equation in terms of the evolving weights, w_j, and nodes (abscissas, or pseudo-components), I_j, of the distribution. Incorporating the Maxwell-Stefan equations into the equations for film theory (steady transport across the film), it is found that the nodes are constant through the film [22], although it is noted here that they may vary temporally if the droplet boundary conditions also vary temporally, as they would in the context of a CFD implementation. One then arrives at a set of equations for the diffusive flux of each *pseudo-component*, J_j, at the droplet surface, that can be written in matrix form, analogous to Eq. (2):

$$\vec{J} = \frac{c_g}{R\left(1-R/R_f\right)}\left[\overline{\overline{D}}\right]\left[\overline{\overline{\psi}}\right]\left(\exp\left[\overline{\overline{\psi}}\right]-\left[\overline{\overline{I}}\right]\right)^{-1}\left(w_{gs}-w_{g\infty}\right) \tag{7}$$

The continuous forms of $\left[\overline{\overline{D}}\right]$, $\left[\overline{\overline{B}}\right]$, and $\left[\overline{\overline{\psi}}\right]$ are analogous to Eqs. (3) – (5), but employ the CA-DQMoM weights at the gas surface, $w_{j,gs}$, and far field, $w_{j,g\infty}$, in place of the mole fractions, x.

In contrast to the DCM, in which all species are solved on both sides of the film, different pseudo-components are present on either side of the film in CA-DQMoM, since on the vapor side of the droplet surface, the nodes ($I_{j,gs}$) are evolving state variables, and at the far-field boundary, the nodes ($I_{j,g\infty}$) vary with the time-dependent boundary conditions as the droplet moves through the Eulerian phase and are calculated in this paper using the Wheeler algorithm. There is, therefore, ambiguity about which pseudo-component (node) fluxes should be solved through the film. Moraes et al. suggest solving for *both* sets of pseudo-component fluxes, while setting the weights of the of the $I_{j,gs}$ nodes to zero at the far-field boundary and setting the weights of the $I_{j,g\infty}$ nodes equal to zero at the surface boundary [22]. This doubles the number of pseudo-components diffusing within the film, but the total number of variables in the film is constant, since one must solve for double the number of weights, but the nodes are constant across the film, as noted above.

2.3.2 Optimized Continuous Distribution Variable

As depicted in the lower path of Fig. 1, a CTM approach that can ***directly*** *predict FG fluxes from (or to) the droplets,* in addition to typical thermophysical properties has been developed [8]. Because CTMs require all properties be interpolated as functions of a distribution variable, the key FGs required by the FGM model must now be correlated with the distribution variable. Typical distribution variables for CTMs, however, like normal boiling temperature, T_{nb}, and MW, cannot correlate key FGs in hydrocarbon fuels. Therefore, to predict FG fluxes in addition to thermophysical/transport properties, an approach using a purely mathematical, distribution variable, *I,* has been developed [8]. Optimization is used to assign a numerical value of I to every

species in the target fuel such that the dependence of all physical properties, *as well as* the number of FGs per molecule (y_{CH3}, y_{CH2}, y_{Benzyl}) on I is polynomial. This pre-processing step is performed once per target fuel. In contrast to typical CTM distribution variables, this *optimized distribution* can correlate FGs, like methylene groups as well as typical thermophysical properties, for all species in the target fuel, from all chemical families [8]. By eliminating the delumping step, this "optimized" or "direct" hybrid model can accommodate any type of nonlinearity in the physical model for droplet vaporization, including the Maxwell-Stefan diffusion submodel (Section 2.1).

2.3.3 Functional Group Matching and Chemical Surrogate

The FGM submodel shown in Fig. 1 uses a set of algebraic equations to convert the CTM representation of droplet vaporization into an adaptive discrete chemical surrogate that can be used by CFD [9]. The FGM submodel was inspired by the findings of Won et al. which demonstrated a link between combustion property targets (CPTs) and functional groups (CH_2, $(CH_2)_n$, CH_3, CH, C, and Benzyl-type) [4]. The FGM submodel calculates the instantaneous composition of the flux of a small chemical surrogate by matching the FGs contained in the vaporization (or condensation) flux predicted by the droplet model using CA-DQMoM [9]. The species employed for the chemical surrogate are n-heptane, n-hexadecane, iso-dodecane, and 1,3,5-trimethylbenzene, but can be easily altered to accommodate different Eulerian phase kinetic mechanisms or other considerations. By matching three key FGs (CH_2, CH_3 and Benzyl-type), the instantaneous CPTs of the surrogate vaporization flux will also match those of the target fuel [4]. The CPTs that largely influence combustion behavior are MW, H/C ratio, DCN, and threshold sooting index (TSI) [4]. The MW and H/C ratio are calculated using linear blending rules and the DCN is calculated from the regression in [4]. Due to lack of experimental data for all 67 species, TSI is not considered.

2.4 Physical-Chemical Surrogate Model

The optimized hybrid method will be compared to the existing state-of-the-art approach to account for preferential vaporization: the physical-chemical surrogate. To this end, a nine-component physical-chemical surrogate was formulated for the target fuel representing Jet-A [8], composed of the same nine components used by Won et al. [4] (with different mole fractions corresponding to the particular target fuel composition used here). The surrogate was formulated to match the DCN, MW, H/C ratio, and distillation curve of the target fuel. Details of the optimization procedure used to formulate the surrogates are provided elsewhere [8]. The advanced distillation curves and CPTs calculated for the 67-component target fuel and surrogate for Jet-A were shown in [8]. Based on the good agreement between the target fuel and the physical-chemical surrogates for the CPTs and the advanced distillation curve, it was concluded that the physical-chemical surrogate represents the standard approach to modeling multicomponent fuels.

3. Results

The full (67 species) DCM with Maxwell-Stefan diffusion is first compared to the full DCM using Fick's law (D_{avg}) to assess the impact of the Maxwell-Stefan formulation. Figure 2(a) shows the total vapor molar flow rate for both models for a 100 μm droplet vaporizing into pure air at 10 bar and 600 K, while Fig. 2(b) shows vaporization at 10 bar and 600 K into an air/fuel mixture, with 0.015 mole fractions of n-octane, n-decane, n-dodecane, n-tetradecane, n-hexadecane, iso-octane, iso-dodecane, toluene, methylpentane and indane. The models produce nearly identical molar fluxes for the pure air case, which provides a degree of code verification (there is no analytical solution for this problem). Condensation occurs at early times in Fig. 2(b) before significant heat up. During this time, there are slight differences in the total fluxes in the

Maxwell-Stefan and Fick's law model. For the full DCM, the (average) CPU time increases by 2348% in going from Fick's law to the Maxwell-Stefan formulation.

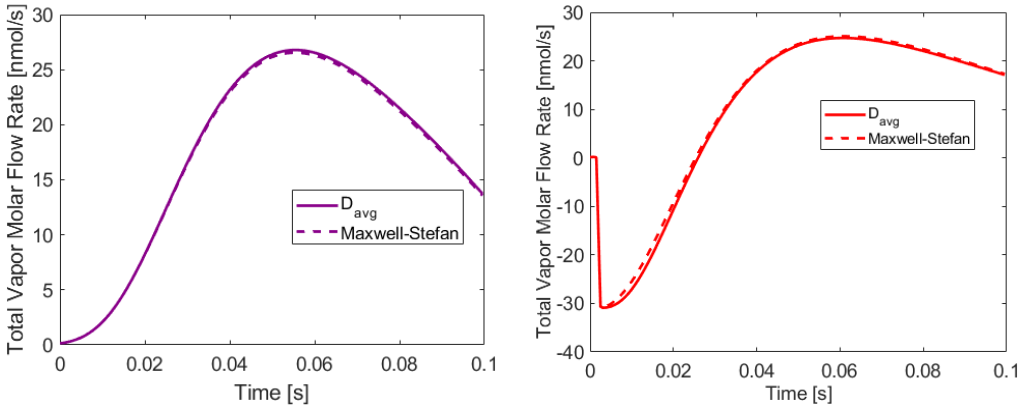

Fig. 2: Vaporization rate for the full DCM using Fick's law ("D_{avg}") and Maxwell-Stefan diffusion model for (a) vaporization into pure air, and (b) vaporization into an air/fuel mixture.

For the case of vaporization in the air/fuel mixture, Fig. 3(a) show individual species fluxes for the six species with the greatest absolute fluxes, and Fig. 3(b) shows the flux of key FGs. Although there are minimal differences in the total flux (Fig. 2(b)), there are notable differences in individual species fluxes. As expected, differences in individual species fluxes to/from the droplet lead to differences in the flux of key FGs to/from the droplet, as seen in Fig. 3(b). This is particularly the case for the CH_2 group, since the condensing species in the air/fuel mixture are primarily n-alkanes and contribute significantly to the flux of the CH_2 group. Differences between the Fick's law and Maxwell-Stefan approaches may become more pronounced at higher pressures and when non-ideal driving forces (i.e., gradients in chemical potential) are considered.

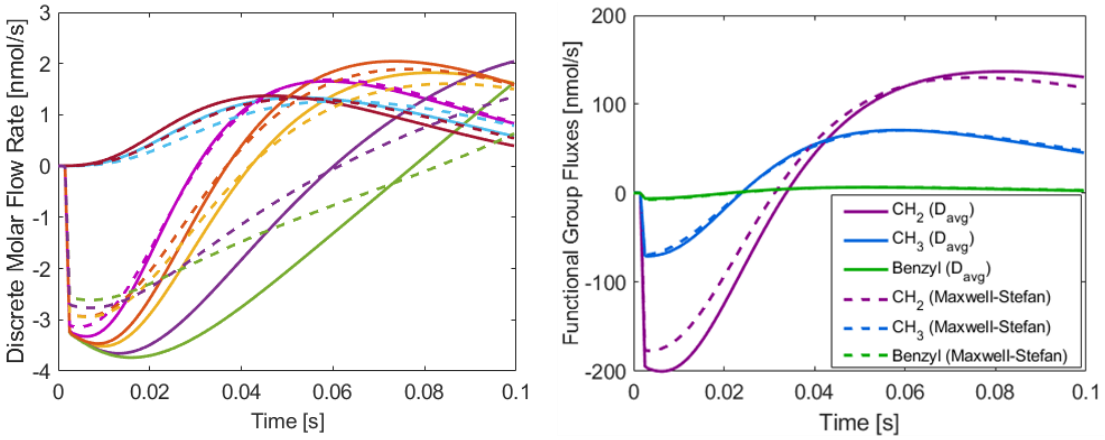

Fig. 3: Comparison of Fick's law (solid lines) and Maxwell-Stefan (dotted lines) models for (a) flux of six discrete species, and (b) FG fluxes, for vaporization into the air/fuel mixture.

The accuracy of the hybrid model with the optimized distribution is next compared to that of the physical-chemical surrogate, with both models incorporating Maxwell-Stefan diffusion and for the air/fuel conditions outlined above. The accuracy is assessed by comparison to the full 67-component DCM (which would be computationally prohibitive for CFD implementations). Figure 4 shows predictions for the evolution of the total droplet vaporization rates. The accuracy of hybrid method and the physical-chemical surrogate method are similar overall, with the surrogate model being more accurate at early times and the hybrid model being more accurate at later times. Both

approaches were of similar accuracy for other physical characterizations of the droplet vaporization process (e.g., surface and average temperatures).

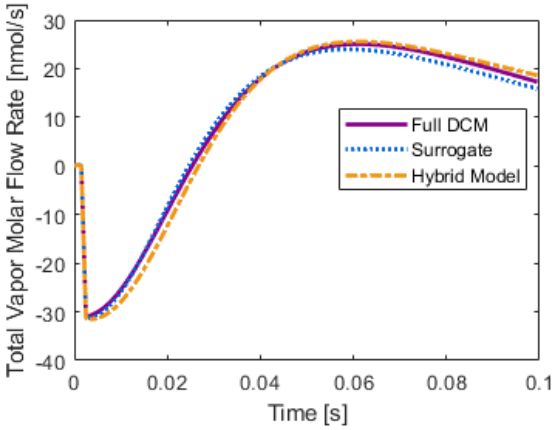

Fig. 4: Total molar flux for the full DCM, physical-chemical surrogate, and the direct hybrid method, all using the Maxwell-Stefan diffusion model.

Differences between the hybrid and the physical-chemical surrogate approaches become more pronounced for instantaneous FG fluxes and the CPTs of those fluxes. The hybrid method with the optimized distribution predicts the H/C ratio and DCN with greater accuracy than the physical-chemical surrogate approach, as seen in Fig. 5(a), while the surrogate method is more accurate for MW. The time-averaged relative errors (compared to the full DCM) in MW, H/C ratio, and DCN were 2.18%, 2.70%, and 8.25% for the physical-chemical surrogate, while they were 5.49%, 1.35%, and 1.92% for the hybrid method, respectively.

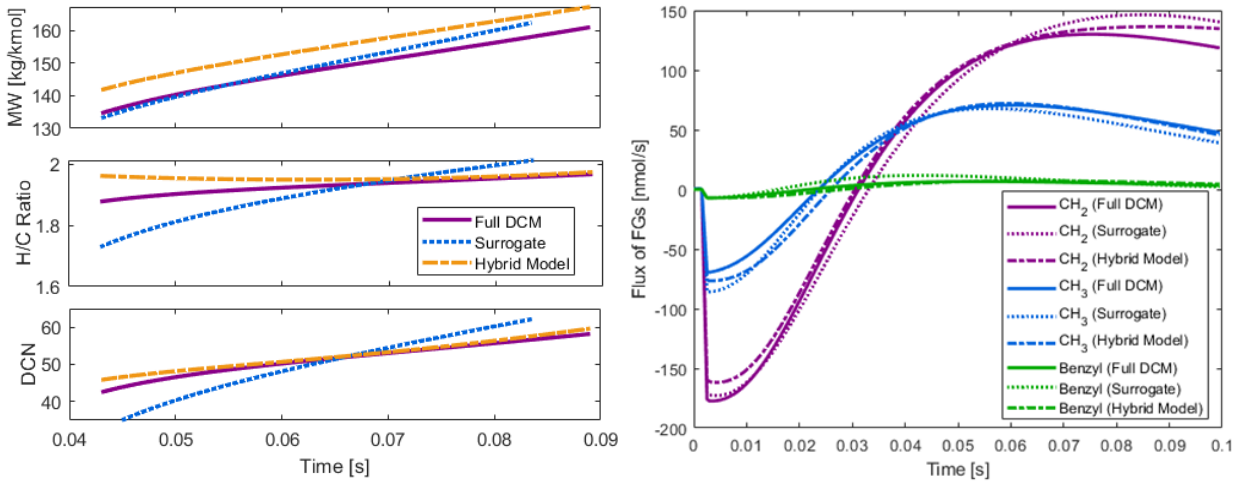

Fig. 5: (a) Instantaneous CPTs of the vaporization flux and (b) flux of FG groups, for the full DCM, physical-chemical surrogate, and the direct hybrid method, all using the Maxwell-Stefan diffusion model.

The hybrid model predicts H/C ratio and DCN with greater accuracy because it predicts the flux of key FGs with greater accuracy, as seen in Fig. 5(b). As demonstrated by Won et al., accurate prediction of the FGs results in accurate prediction of the CPTs [4]. Beyond 0.02 s, the physical-chemical surrogate is less accurate in its predictions of the flux of methylene and benzyl groups than the hybrid method, as in [8].

4. Discussion and Conclusions

For the moderate pressure conditions tested, multicomponent droplet vaporization with Fick's law diffusion and with Maxwell-Stefan diffusion in the boundary layer yield similar predictions for total vaporization rates, but differences in individual species fluxes and FG fluxes. The Maxwell-Stefan diffusion model was then incorporated in a CTM context (CA-DQMoM) for droplet vaporization for the first time, and the hybrid droplet vaporization-adaptive surrogate model was compared to the prevailing physical-chemical surrogate approach. Both methods exhibited similar accuracy in predicting droplet vaporization rates, the surrogate was more accurate in predicting MW, and the hybrid approach was more accurate in predicting instantaneous H/C, DCN, and FG fluxes. The reason for the latter is that physical-chemical surrogates are formulated to match a target fuel's pre-vaporized CPTs and its distillation curve, but nothing constrains the CPTs or FG distribution to vary *along* the distillation curve in the same manner as the target fuel. In contrast, for the hybrid model, FG distributions and all properties relevant to vaporization are correlated with the *same optimized distribution variable*, ensuring that FGs and CPTs match those of the target fuel throughout the droplet's lifetime.

5. Acknowledgments

This research was partially supported by the NSF (Award Number CBET-2140141).

6. References

[1] T.M. Lovestead, J.L. Burger, N. Schneider, T.J. Bruno, Comprehensive Assessment of Composition and Thermochemical Variability by High Resolution GC/QToF-MS and the Advanced Distillation-Curve Method as a Basis of Comparison for Reference Fuel Development, Energy and Fuels. 30 (2016) 10029–10044. doi:10.1021/acs.energyfuels.6b01837.

[2] S.H. Won, N. Rock, S.J. Lim, S. Nates, D. Carpenter, B. Emerson, T. Lieuwen, T. Edwards, F.L. Dryer, Preferential vaporization impacts on lean blow-out of liquid fueled combustors, Combust. Flame. 205 (2019) 295–304. doi:10.1016/j.combustflame.2019.04.008.

[3] S.J. Lim, A.K. Alwahaibi, F.L. Dryer, S.H. Won, Impacts of preferential vaporization on flashback behaviors of multi-component liquid fuels, Combust. Flame. 245 (2022) 112300.

[4] S.H. Won, F.M. Haas, S. Dooley, T. Edwards, F.L. Dryer, Reconstruction of chemical structure of real fuel by surrogate formulation based upon combustion property targets, Combust. Flame. 183 (2017) 39–49. doi:10.1016/j.combustflame.2017.04.032.

[5] D. Kim, J. Martz, A. Abdul-Nour, X. Yu, M. Jansons, A. Violi, A six-component surrogate for emulating the physical and chemical characteristics of conventional and alternative jet fuels and their blends, Combust. Flame. 179 (2017) 86–94. doi:10.1016/j.combustflame.2017.01.025.

[6] O.S. Abianeh, M.A. Oehlschlaeger, C.-J. Sung, A surrogate mixture and kinetic mechanism for emulating the evaporation and autoignition characteristics of gasoline fuel, Combust. Flame. 162 (2015) 3773–3784. doi:10.1016/j.combustflame.2015.07.015.

[7] H. Wang, R. Xu, K. Wang, C.T. Bowman, R.K. Hanson, D.F. Davidson, K. Brezinsky,

F.N. Egolfopoulos, A physics-based approach to modeling real-fuel combustion chemistry - I. Evidence from experiments, and thermodynamic, chemical kinetic and statistical considerations, Combust. Flame. 193 (2018) 502–519. doi:10.1016/j.combustflame.2018.03.019.

[8] S.L. Singer, M.P. Hayes, A.Y. Cooney, A hybrid droplet vaporization-adaptive surrogate model using an optimized continuous thermodynamics distribution, Fuel. 288 (2021) 119821. doi:10.1016/j.fuel.2020.119821.

[9] A.Y. Cooney, S.L. Singer, A hybrid droplet vaporization-chemical surrogate approach for emulating vaporization , physical properties, and chemical combustion behavior of multicomponent fuels, Proc. Combust. Inst. 3 (2019) 3229–3236.

[10] A.Y. Cooney, S.L. Singer, Modeling Multicomponent Fuel Droplet Vaporization with Finite Liquid Diffusivity using Coupled Algebraic-DQMoM with Delumping, Fuel. 212 (2018) 554–565. doi:10.1016/j.fuel.2017.10.056.

[11] G. Castiglioni, J. Bellan, On models for predicting thermodynamic regimes in high-pressure turbulent mixing and combustion of multispecies mixtures, J. Fluid Mech. 843 (2018) 536–574. doi:10.1017/jfm.2018.159.

[12] B. Abramzon, W.A. Sirignano, Droplet vaporization model for spray combustion calculations, Int. J. Heat Mass Transf. 32 (1989) 1605–1618. doi:10.1016/0017-9310(89)90043-4.

[13] T. Runge, M. Teske, C. Polymeropoulos, Low Temperature Vaporization of JP-4 and JP-8 Fuel Droplets, At. Sprays. 8 (1998) 25–44.

[14] H. Nomura, Y. Ujiie, H.J. Rath, J. Sato, M. Kono, Experimental study on high-pressure droplet evaporation using microgravity conditions, Symp. Combust. 26 (1996) 1267–1273. doi:10.1016/S0082-0784(96)80344-4.

[15] R. Taylor, R. Krishna, Multicomponent Mass Transfer, Wiley, 1993.

[16] P. He, A. Raghavan, A.F. Ghoniem, Impact of non-ideality on mixing of hydrocarbons and water at supercritical or near-critical conditions, J. Supercrit. Fluids. 102 (2015) 50–65. doi:10.1016/j.supflu.2015.03.017.

[17] S. Tonini, G.E. Cossali, A multi-component drop evaporation model based on analytical solution of Stefan-Maxwell equations, Int. J. Heat Mass Transf. 92 (2016) 184–189. doi:10.1016/j.ijheatmasstransfer.2015.08.014.

[18] H.L. Toor, Solution of the Linearized Equations of Multicomponent Mass Transfer, AIChE J. 10 (1964) 448–455.

[19] W.E. Stewart, R. Prober, Matrix Calculation of Multicomponent Mass Transfer in Isothermal Systems, Ind Eng. Chem., Fundam. 3 (1964) 224–235.

[20] J.T. Edwards, Reference Jet Fuels for Combustion Testing, 55th AIAA Aerosp. Sci. Meet. (2017) 1–58. doi:10.2514/6.2017-0146.

[21] P.B. Govindaraju, M. Ihme, Group contribution method for multicomponent evaporation with application to transportation fuels, Int. J. Heat Mass Transf. 102 (2016) 833–845. doi:10.1016/j.ijheatmasstransfer.2016.06.079.

[22] A.O.S. Moraes, P.L.C. Lage, L.F.L.R. Silva, Mass transfer in continuous mixtures with Maxwell-Stefan diffusion using the adaptive characterization method, AIChE J. 66 (2020) e16852.

13th U.S National Combustion Meeting
Organized by the Central States Section of the Combustion Institute
March 19-22, 2022
College Station, Texas

High-Speed Visualization of Precursor Droplet Evaporation in Flame Assisted Spray Pyrolysis of NCM811 Battery Cathodes

Maanasa Bhat[1], Jianan Zhang[1], Chuwei Zhang[1], Sili Deng[1]*

[1]Department of Mechanical Engineering, Massachusetts Institute of Technology
**Corresponding Author Email: silideng@mit.edu*

Abstract: The performance of the Li-ion battery is known to be dependent on structure, composition and morphology of the constituent cathode and anode materials. Flame Assisted Spray Pyrolysis (FASP) is an attractive prospect for manufacturing Li-ion battery cathodes owing to its simplicity and low cost. FASP includes two stages: (1) the initial heating stage where the precursor droplet evaporates and partially decomposes, and (2) the final decomposition stage where it goes through the flame to form a fully decomposed oxide particle. In order to ensure superior control over the product structure, a detailed understanding of the phenomena occurring during these two stages is vital. In this work, we use high speed visualization to examine the trajectory of a single precursor droplet as it goes through the FASP process. The focus is on the evaporation behaviour in the initial heating stage of the process before the precursor enters the flame. The evaporation of the droplet is investigated using a custom-built setup that includes a heating chamber enclosing the suspended precursor droplet. The precursor chosen is a mixture of water with lithium, nickel, manganese, and cobalt nitrates in the mole ratio 1.1:0.8:0.8:0.1 which is a commonly used precursor for battery cathode material $LiNi_{0.8}Co_{0.1}Mn_{0.1}O_2$ (NCM811). Qualitative and quantitative analyses were conducted on the obtained data to determine evaporation rate and identify morphological changes. The effect of the precursor additive urea (2.5% by weight) was explored for controlling product particle structure and morphology. It was found that the urea decomposition reaction occurring at ~ 150 ^{0}C plays a very important role in obtaining uniform precursor salt distribution in the product particle ensuring minimal post-processing of synthesized NCM811 cathode materials. The results from this study show that the final product structure is largely determined by the processes occurring at the initial heating stage of the FASP process. Therefore, it might be beneficial for any process design modifications targeting product structure improvement to be focused on this stage.

Keywords: *Flame Assisted Spray Pyrolysis, Li-ion batteries, Single-droplet evaporation, Product morphology control*

1. Introduction

Li-ion batteries have become increasingly popular in the recent years for use in electric vehicles and energy storage. The batteries are expected to be highly efficient with a large capacity, good cyclic retention rate and high energy density. This performance of the battery is dependent on the structure, composition and morphology of the constituent cathode and anode materials. One of the biggest hurdles is economical manufacturing of battery cathodes and anodes while maintaining the required high-performance standards. Cathode manufacturing in particular, is known to constitute ~ 40% of the total battery manufacturing cost [1-2].

Currently, cathode materials are manufactured using co-precipitation, hydrothermal or sol-gel methods [3]. These processes are time consuming; taking anywhere between 10-24 h to complete the multiple steps. The synthesized cathode materials are then made to undergo another 5-10 h of post processing heat treatment before they can be assembled into a battery cell. This makes cathode manufacturing highly expensive.

Flame Assisted Spray Pyrolysis (FASP) is a combustion-based manufacturing process which combines spray drying and flame synthesis to obtain micron sized product particles of desired morphology [4]. A two stage FASP method for manufacturing nickel rich $LiNi_{0.8}Co_{0.1}Mn_{0.1}O_2$ (NCM811) cathode materials was developed in our laboratory by Zhang et al. [5]. Here, the droplets atomised using an ultrasonic atomizer go through two stages: (1) the initial heating stage where the droplets pass through a heated tube maintained at temperature ~ 170-230 ^{0}C and (2) the final decomposition stage where the partially decomposed particles exiting from the heated tube go through a premixed methane flame for full decomposition and are later collected using a filter. The collected particles from this FASP setup were annealed at 750 ^{0}C for ~ 10 h to obtain fully crystallised cathode material. Interestingly, it was observed that addition of a small amount of urea to the precursor solution produced particles that needed only ~ 20 mins of annealing time at 875 ^{0}C temperature to be fully crystallised and battery ready. It was hypothesized that addition of urea causes a change in the droplet evaporation process in the initial heated section that improves the particle morphology favoring reduced post processing heat treatment time [5].

Such an order of magnitude reduction in a part of the synthesis process has the potential to drastically reduce the cost of cathode manufacturing and a possibility of eventually omitting the heat treatment step itself. It is necessary to obtain a fundamental understanding of the droplet evaporation process occurring in the heated section in order to apply any design modifications for improved product particle morphology. In this paper, we used high speed visualization to look at single precursor droplet evaporation process during the initial heating stage at various temperatures. Continuing our studies from Zhang et al. [5], we investigated the effect of the additive urea to the NCM811 cathode precursor solution. The data were qualitatively and quantitatively analysed to enhance our understanding of the product particle formation process in FASP.

2. Materials and Methods

The single drop visualization setup is shown in Fig. 1. It consists of a rectangular stainless-steel chamber heated to desired temperature using four ceramic heaters (Ceramix infrared heating element, 125W) fixed on two walls. The temperature is controlled using a PID temperature controller. The other two walls are fixed with optical windows made of quartz to facilitate viewing. The chamber is covered on top with a plate that has an attached thermocouple. The aluminium holder is used to support a cross fiber arrangement of SiC wires (Silicon carbide, 16 μm diameter, NGS Advanced Fibers Co., Ltd.). The holder is attached to a beam which is capable of vertical movement using an Arduino controlled motor. The holder itself is also capable of independent vertical movement and this is used to move the droplet in and out of the cylindrical quartz protector which is used to shield the droplet from the high chamber temperature before recording. The camera used is Phantom V4.2 (512 x 512 pixels) and the frame rate is set at 10 fps. An arrangement of different optical elements (Nikkor 35-105mm /3.5-4.5 lens, 300 mm double concave lens, Edmund Optics MX-5 objective) is used to enhance the magnification and improve image resolution. The measured final resolution of the setup is 100 pixels/mm.

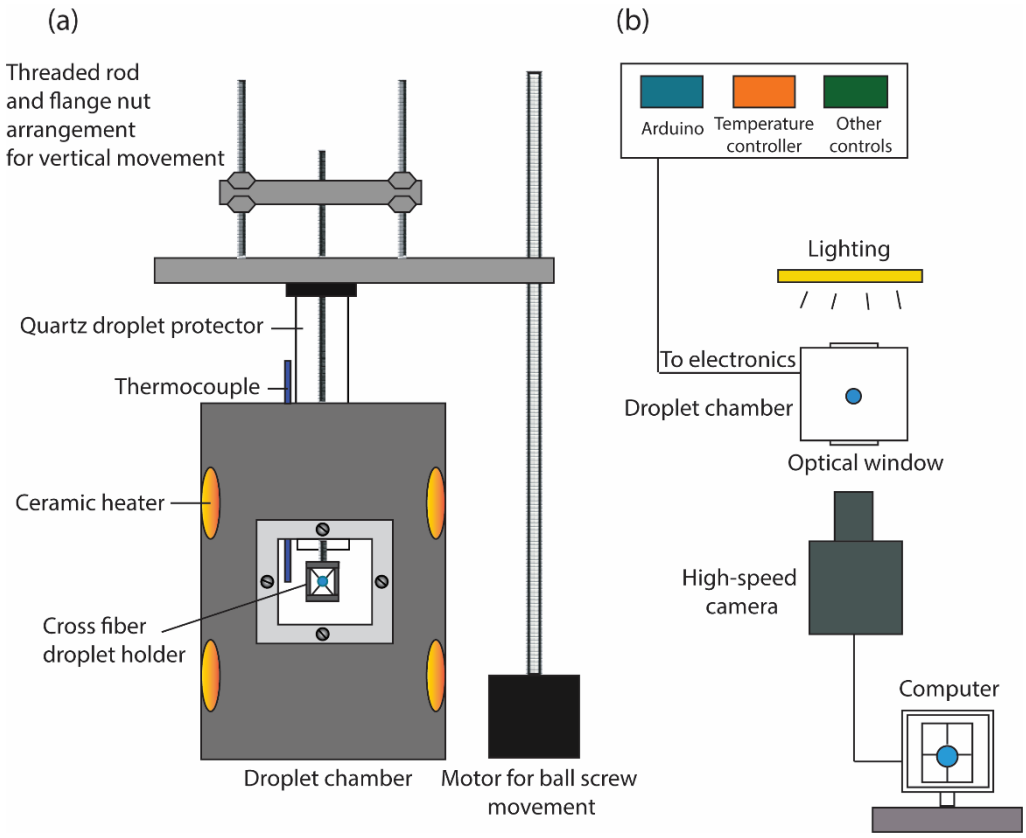

Figure 1: Schematic of (a) droplet heating chamber and (b) camera arrangement for visualization of single droplet evaporation

The precursor solution used is a mixture of nickel nitrate hexahydrate ($Ni(NO_3)_2.6H_2O$), cobalt nitrate hexahydrate ($Co(NO_3)_2.6H_2O$), manganese nitrate tetrahydrate ($Mn(NO_3)_2.4H_2O$) and lithium nitrate ($LiNO_3$) in the molar ratio 0.8:0.1:0.1:1.1 dissolved in water to obtain a final concentration of 2 mol/L. This is referred to as the NCM solution. 2.5 wt% urea (Sigma-Aldrich, > 99.5%) is added to the NCM solution to get the NCM-urea solution. A syringe pump (New Era NE-300) is used to obtain droplets of narrow size distribution (400-600 μm). The droplets are made to fall on the horizontally placed aluminium holder and attach to the intersection of the SiC cross fibers. The syringe needle is coated with hydrophobic coating (NeverWet Rust-oleum) to ensure easy detachment of droplets from needle tip to cross fiber arrangement. The holder is then carefully fixed to the lever and moved inside the chamber to begin recording.

The recorded videos are processed to extract images that can be used for further analysis. Diameter of the droplet is measured using an in-house MATLAB image processing code that maps the edges of the droplet. Diameter is measured in horizontal and vertical directions and averaged to obtain the final diameter.

3. Results

As a first step towards understanding the processes occurring in the initial heated section, it was vital to obtain particles at the exit of the section. However, the current configuration of the FASP setup as given in Zhang et al. [5] did not allow for mid-process particle collection. Hence, a simple reconstruction of the heated section was made by placing a steel tube inside a tube furnace and passing atomized droplets through the tube (Fig. 2a). The furnace temperature was

set at 225 ^{0}C which is in the typical range of temperatures used in the FASP setup. Droplets of NCM and NCM-urea precursor solutions were produced using an ultrasonic atomizer and carried to the furnace tube using 0.1 lpm oxygen as carrier gas. The particles produced in the tube were collected using a filter and vacuum pump arrangement at the exit. The collected particles for NCM and NCM-urea cases are shown in Fig. 2b and Fig. 2c respectively.

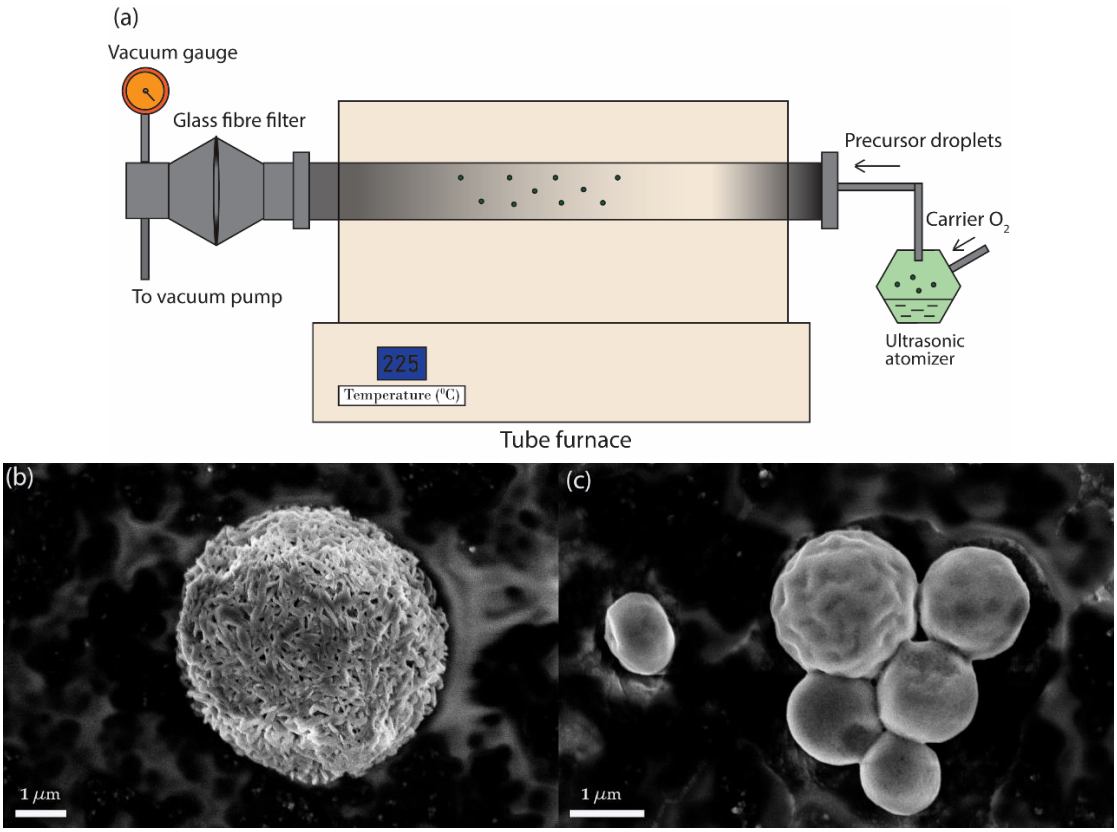

Figure 2: (a) Schematic of the simple tube setup for mimicking the heated section of FASP, (b, c) Particles collected at exit of heated section for (b) NCM precursor solution (c) NCM-urea precursor solution.

It can be observed that the morphology of the particles is drastically different for both cases. For NCM (Fig. 2b), the particles seem to be made up of several needle-shaped structures joined together to form a spherical shape. In contrast, the NCM-urea particles (Fig. 2c) have a smoother surface with occasional wrinkling and no needle-shaped structures. These results indicated that addition of urea had a significant impact on the droplet evaporation process in the heated section causing the end products to have varying morphologies. The morphological differences also raised several questions about the significance of the heated section in the FASP particle formation process. To further elucidate the effect of urea addition on the processes occurring in the heated section, visualization of the droplet evaporation process was done using a high-speed camera.

The specifics of the visualization experiments have been detailed in the previous section. As discussed, NCM and NCM-urea precursor droplets of size ~ 400-600 μm were placed on SiC cross fiber and imaged using a high-speed camera. The frames extracted from the videos for different temperature conditions are given in Fig. 3 and the corresponding diameter evolution history is given in Fig. 4. The phenomena occurring at different temperatures are discussed in detail in the following paragraphs.

Sub-topic: Droplet and Sprays

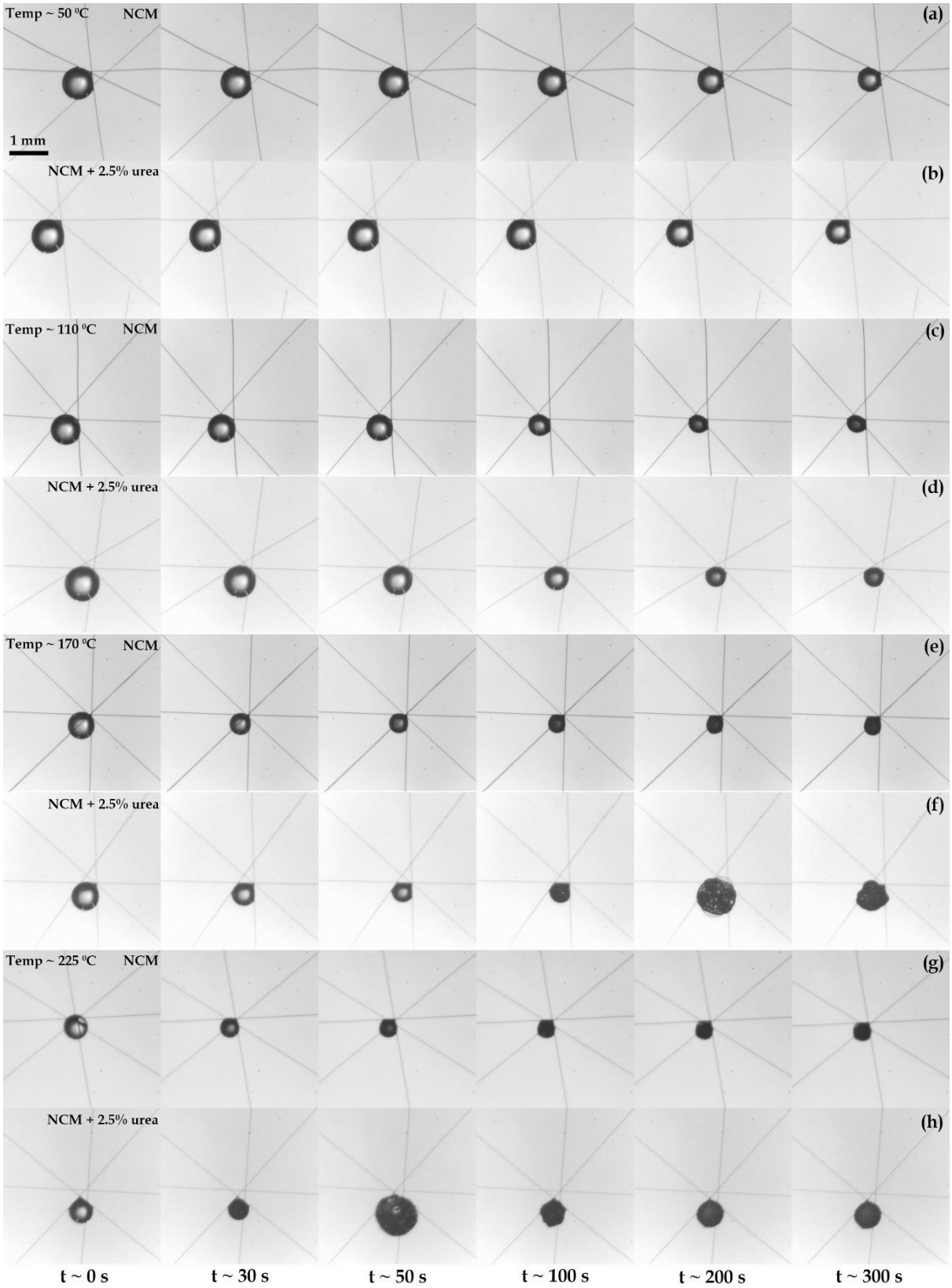

Figure 3: (a-h) Images of single droplet evaporation for NCM and NCM-urea precursors at different temperatures (a, b) 50 ^{0}C , (c, d) 110 ^{0}C, (e, f) 170 ^{0}C and (g, h) 225 ^{0}C

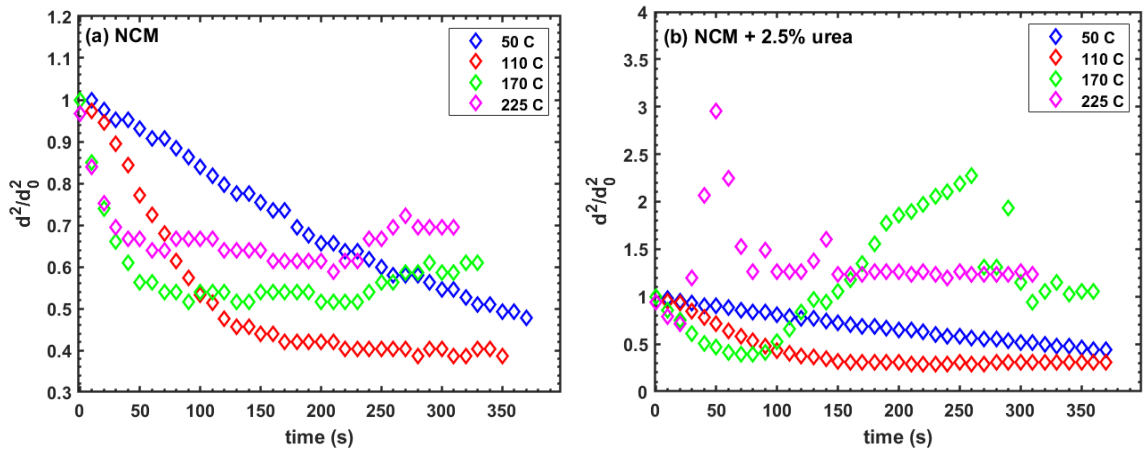

Figure 4: Variation of non-dimensional droplet diameter with time for droplets of (a) NCM precursor solution (b) NCM-urea precursor solution

Temperature ~ 50 ^0C: The behaviours of both NCM and NCM-urea droplets are found to be similar at this temperature (Fig. 3a and Fig. 3b). There is a continuous decrease in droplet diameter with time as indicated by blue symbols in Fig. 4a and Fig. 4b. The decrease is found to be linear implying $d^2 \sim t$ which is the well-known *d^2 law* for evaporation of a spherical drop [6]. The evaporation rate (approximate estimate from the slope of the straight line) is found to be the same for both NCM and NCM-urea solutions. No bubble formation or boiling is observed as temperature is below the boiling point of the solvent (water).

Temperature ~ 110 ^0C: At this temperature, the droplet evaporation behaviour is initially similar to 50 ^{0}C. There is a continuous decrease in droplet size with time as shown in Fig. 4a and Fig. 4b with red symbols. However, at ~ 100 s the evaporation begins to slow down and starts to deviate from the *d^2 law*. By ~ 150 s the evaporation almost stops completely, and the droplet size is found to be constant for the next ~ 200 s. This could be attributed to the movement of the precursor salts (solute) within the droplet. As temperature increases, water (solvent) evaporates which causes the salts to precipitate and form a layer at the droplet surface [7]. Eventually the salt layer is thick enough that the rest of the solvent is trapped inside and there is no more change in droplet size. The increase in thickness of salt layer can also be observed in the images Fig. 3c and Fig. 3d where the black edge of the droplet is increasing in thickness as the droplet size decreases.

Temperature ~ 170 ^0C: At this stage, NCM and NCM-urea droplets start to differ in their evaporation behaviour. The NCM droplet (Fig. 3e) shows the expected decrease in droplet size up to ~ 100 s and then remains constant for another 100 s more before showing a slight increase at the ~ 220 s mark (Fig. 4a, green symbols). This slightly delayed increase in droplet diameter can be attributed to bubble formation and expansion from inside the droplet due to the temperature of the trapped solvent reaching boiling point. The bubbles are faintly visible in the images shown in Fig. 4e. A similar darkened edge of the droplet is also seen indicating water evaporation and possible salt precipitation. The NCM-urea droplet shown in Fig. 3f starts the same as NCM droplet with a sharp decrease in droplet size for ~ 100 s and then starts to expand rapidly. The expansion is heralded by the appearance of multiple bubbles or vapor pockets inside the droplet that cause it to suddenly increase in size and distort in shape. The vapor pockets form and collapse rapidly causing the droplet diameter to oscillate in a highly erratic

fashion (Fig. 4b). After a long period of rapid expansion and collapse the droplet settles down into a spherical shape with no more distortions.

Considering this rapid expansion and collapse phenomenon is unique to the NCM-urea droplet, it can be deduced to be caused due to a physical or chemical phenomenon involving the urea additive. As NCM droplet images suggest, any internal bubble formation due to the boiling solvent would only result in a small increase in size and not the violent expansion observed here. Looking at the properties of urea, it can be observed that upon reaching a temperature of ~ 150 ^{0}C urea is known to decompose into ammonia and isocyanic acid both of which are in vapor form [8]:

$$NH_2 - CO - NH_2(l\ or\ g) \rightarrow NH_3(g) + HNCO(g) \qquad (1)$$

The vapor pockets formed in the droplet can be speculated to be products of urea decomposition. The significant effect of the rapid expansion and collapse process is the creation of a disturbance to the surface salt precipitation process. This leads to the salts now being distributed more uniformly within the droplet as opposed to only at the surface. This hypothesis could explain the morphology of the particles collected at the exit of the heated section shown in Fig. 2b and Fig. 2c. The needle shaped structures observed in NCM particles are salt precipitates that are present at the surface of the droplet. The structures are not visible for NCM-urea particles as the precursor salts are uniformly mixed within the particles.

Temperature ~ 225 ^{0}C: This is the temperature close to the range used in the heated section of the FASP setup. It can be observed that the evaporation behaviour is similar to the phenomenon described for 170 ^{0}C in the previous section but occurs at a faster rate (Fig. 3g, Fig. 3h and Fig. 4). NCM droplet shows initial linear decrease in droplet size and slight increase at the later stages with formation of bubbles inside the droplet. NCM-urea droplet shows the rapid expansion and collapse behaviour indicative of urea decomposition occurring in the droplet.

The results from SEM characterization of particles collected at exit of heated section (Fig. 2) as well as the high-speed imaging (Fig. 3 and Fig. 4) help to provide a clearer understanding of the evaporation process occurring in the heated section. As the NCM droplet enters the heated section at temperature ~ 225 ^{0}C, the solvent begins to evaporate. This causes a precipitation of salts at the surface which eventually forms a shell around the droplet and when this particle moves through the flame it decomposes to form oxide particles. This process is disrupted by the addition of urea as it decomposes at ~ 150 ^{0}C causing the droplet to undergo rapid expansion and collapse several times. This violent phenomenon causes the precursor salts to mix uniformly and prevent precipitation at the surface. Further characterization of elemental distribution of the resulting particles as well as computational single droplet models are being used to validate the hypothesis.

4. Conclusions

High speed visualization was used to improve fundamental understanding of the droplet evaporation process occurring in the heated section of FASP setup. The effect of urea as an additive to NCM precursor solution was explored and it was found that urea decomposition reaction at ~ 150 ^{0}C causes rapid expansion and collapse of the droplet possibly leading to uniform mixing of precursor salts. Temporal variation of the droplet diameter was determined, and it was found that it deviates from d^2 *law* at longer times due to potential formation of salt precipitates on the surface of the droplet. For future work, elemental distribution of the different

precursor salts in the resultant product particle will be investigated to further enhance our knowledge of the evaporation process.

5. Acknowledgements

The authors would like to thank Valerie Muldoon and Dr. Yuesen Wang for their contribution in designing and building the experimental setup. The authors acknowledge the support from Centre for Mechanical Engineering Research and Education at MIT and SUSTech. MB is partially supported by the MathWorks Mechanical Engineering Fellowship.

6. References

[1] A. Manthiram, A reflection on lithium-ion battery cathode chemistry, Nat. Commun. 11 (2020) 1–9.

[2] K. Turcheniuk, D. Bondarev, G.G. Amatucci, G. Yushin, Battery materials for low-cost electric transportation, Mater. Today. 42 (2021) 57–72.

[3] Z. Chen, W. Zhang, Z. Yang, A review on cathode materials for advanced lithium ion batteries: Microstructure designs and performance regulations, Nanotechnology. 31 (2020).

[4] S. Li, Y. Ren, P. Biswas, S.D. Tse, Flame aerosol synthesis of nanostructured materials and functional devices: Processing, modeling, and diagnostics, Prog. Energy Combust. Sci. 55 (2016) 1–59.

[5] J. Zhang, V.L. Muldoon, S. Deng, Accelerated synthesis of Li(Ni0.8Co0.1Mn0.1)O2 cathode materials using flame-assisted spray pyrolysis and additives, J. Power Sources. 528 (2022) 231244.

[6] C.K. Law, Recent advances in droplet vaporization and combustion, 8 (1982) 171–201.

[7] Y. Ren, J. Cai, H. Pitsch, Theoretical Single-Droplet Model for Particle Formation in Flame Spray Pyrolysis, Energy and Fuels. 35 (2021) 1750–1759.

[8] T.J. Wang, S.W. Baek, S.Y. Lee, Experimental Investigation on Evaporation of Urea-Water-Solution Droplet for SCR Applications, AIChE J. 55 (2009) 3267–3276.

13th U. S. National Combustion Meeting
Organized by the Central States Section of the Combustion Institute
March 19–22, 2022
College Station, Texas

Ignition enhancement of liquid ammonia sprays under engine-relevant conditions via ambient hydrogen addition

Ahmad Hadi Bakir[1], Haiwen Ge[2], Zhili Zhang[1], Peng Zhao[1]*
[1] Department of Mechanical, Aerospace & Biomedical Engineering, UT Space Institute, University of Tennessee, Knoxville, TN 37388 USA
[2] Department of Mechanical Engineering, Texas Tech University, Lubbock, TX, USA
**Corresponding author email: pzhao12@utk.edu*

Abstract: With the growing trend in decarbonization of ground transportation, low and zero-carbon fuels have attracted extensive research interest. Liquid ammonia is a promising alternative fuel due to its high volumetric energy density, mature production and distribution infrastructure, convenience of storage, and zero carbon emissions. However, ammonia combustion also suffers from low flame speed and weak chemical reactivity. In this work, we computationally investigate the suitable engine-relevant thermochemical conditions for auto-ignition of constant volume ammonia spray, as well as its spray dynamics, vaporization, flash boiling effects, and emissions. The simulation is first validated by comparing against available experimental data from a vaporizing ammonia spray, and then extended to chemically reactive conditions. Results show that ammonia sprays under engine relevant condition (60 bar and 1200K) can only successfully auto-ignite for cases with hydrogen addition, due to enhancement of thermal condition and chemical reactivity. A chemical flux analysis is conducted to further understand the important species and reactions that promote ammonia auto-ignition from hydrogen, which potentially can be introduced via H_2 solubility, exhaust gas recirculation, and on-board ammonia thermal decomposition. Furthermore, results have indicated that charge cooling effects can further decrease the temperature in the flow field and make auto-ignition more difficult. This study provided useful insights for the application of ammonia as a zero-carbon fuel for ground transportation.
Keywords: Liquid ammonia, spray, hydrogen addition, autoignition, flash boiling, charge cooling

1. Introduction

Ground transportation heavily relies on high energy density liquid fuels. With more and more stringent regulations on greenhouse gas (GHG) emissions, research and development on low and zero-carbon transportation fuels have attracted extensive interest [1]. As such, the focus has shifted towards ammonia and hydrogen due to their carbon-free combustion process. Liquid ammonia (NH_3), provides a volumetric energy density of 11.5 MJ/L, a widely developed production and transportation infrastructure. Ammonia can be effectively synthesized through the well-known Haber-Bosch process at low cost from water and nitrogen [2]. However, as an engine fuel, ammonia has a very low flame speed around 7 cm/s under 1 atm and 298 K, which is only around 20% of the flame speed of gasoline and hence has a limited heat release rate in spark ignition engines. The low flame speed also leads to easier near-wall quenching and incomplete combustion resulting in ammonia slip [3]. Furthermore, the ignition delay of ammonia is substantially longer than gasoline and diesel under similar thermodynamic conditions, limiting its application to high-load and low-speed engines.

The combustion performance of ammonia can be substantially improved when interacting with other fuels, such as H_2 [4]. H_2 can be directly made through partial thermal or catalytical cracking with ammonia [5] to achieve desired flame speed enhancement. From the application perspective,

ammonia combustion will be benefited through the direct injection in its liquid phase, to take advantage of its higher volumetric energy density and convenience of storage and delivery. Meanwhile, compression ignition engines, which traditionally use direct injection, allow high compression ratio and thermal efficiency for ammonia combustion. Unfortunately, high-pressure liquid ammonia combustion, especially under spray-related conditions, are insufficiently investigated.

In this study, we computationally investigate the spray behavior of liquid ammonia under both vaporization-only and autoignition conditions. The emphasis is placed on the ignition enhancement of ammonia spray via H_2 doping in the ambient gas. Three effects including the thermal and chemical effects from H_2 addition, and the contradictory effect from ammonia charge cooling are separately discussed to inform ammonia spray autoignition. The results will provide useful insights on the application of liquid ammonia in direct injection compression ignition engines and other ammonia-powered spray combustion systems.

2. Numerical Methodology

2-1. Numerical models

The commercial computational fluid dynamics (CFD) software CONVERGE^{TM} [6] is employed to simulate the spray processes. A Redlich-Kwong equation of state is utilized to describe the two-phase fluid. Fuel injection is modeled through the blob injection model. Secondary break-up of the spray is modeled using the Kelvin-Helmholtz Rayleigh-Taylor (KH-RT) models [7]. No-Time-Counter collision model is considered for the droplet interactions [8]. Drag effects are considered using the dynamic drop drag model, with the O'Rourke turbulent dispersion model [9] and the Frossling model for droplet evaporation. Turbulence is modeled by the Reynolds-Averaged Navier-Stokes (RANS) models. Both standard k-ε model and Renormalization Group (RNG) k-ε model are considered [10]. The SAGE chemistry solver is used for the combustion process [11]. A base mesh size of 4 mm is selected with an adaptive mesh refinement embedding level of 5 that is enabled based on velocity and temperature gradients. Furthermore, a level 5 fixed embedding around the injector is used as well to capture the velocity changes from liquid to gas.

Table 1: set-up of the ammonia spray

Injection					Ambient Conditions			Fuel	Volume	Spray angle
Diameter	Pressure	Temp.	Duration	Mass	Temp.	Gas	Pressure			
0.365 mm	120 Bar	293 K	3.9 ms	297 mg	293 K	Air	2 Bar	Liquid ammonia (293K)	2.5 L	65 degrees

2-3. Validation of a vaporizing ammonia spray

A spray experiment conducted by Pele et. al. [12] will be considered for the validation of the numerical models, liquid ammonia is injected by gasoline direct injection (GDI) injector in a constant volume chamber. The validation target selected has an injection duration of 3.9 ms with fuel temperature and injection pressure of 293 K and 120 bar, respectively. Due to the low boiling point of ammonia, flash boiling may occur in the ammonia spray and requires special consideration. The flash boiling forms bubbles inside the bulk liquid that continue to grow with the development of the spray. Once the bubbles erupt, a collapsing spray is formed by the interaction of the wider individual plumes in the spray. Consequently, this leads to fast evaporation

of the droplets and reduction in momentum [13]. The simulation further adopts the flash boiling model in [14] that involves a droplet size reduction scale parameter and a heat transfer coefficient scale parameter. The configurations and operating parameters of the ammonia spray experiment are listed in Table 1.

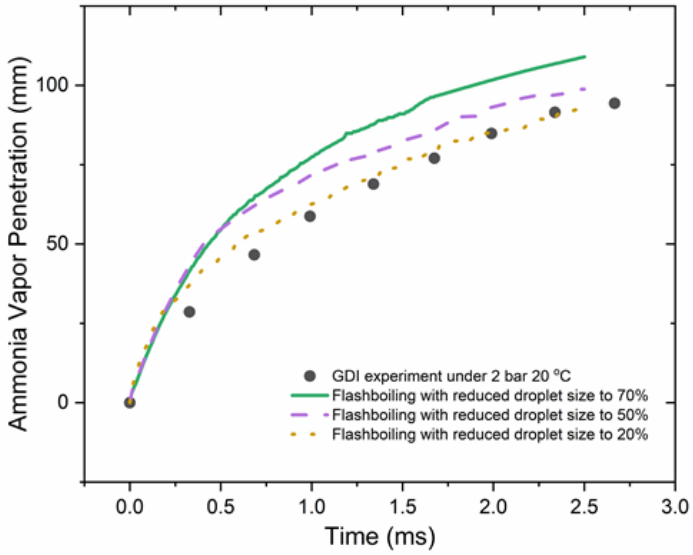

Figure 1: Vapor penetration of liquid ammonia comparison between experiment and numerical results at different reduced droplet size scales.

Numerical simulations are validated against the vapor penetration of the ammonia spray experiment with flash boiling. Figure1 shows the vapor penetration comparison of the numerical results at different droplet size reduction scales with the experimental data. The 20% droplet size reduction shows the best agreement with the vapor penetration distance from the experiment compared to the 50% and 70% cases. However, the 70% case is selected to show for this work. This decision can be explained by studying the spray morphology.

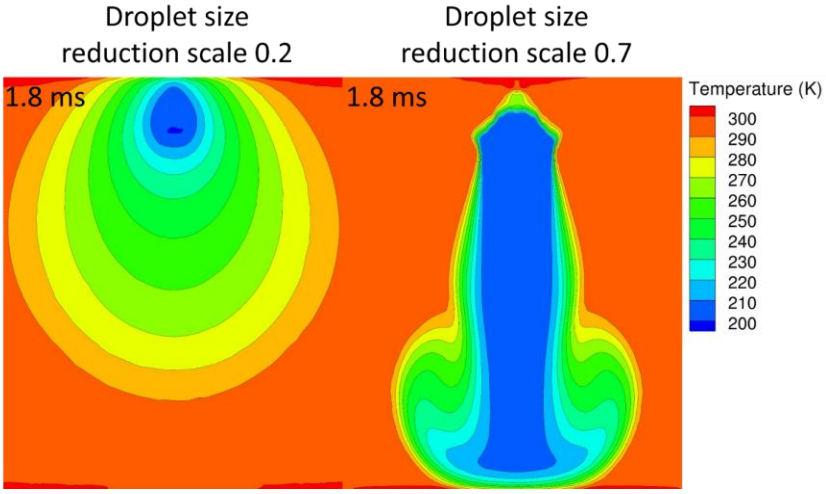

Figure 2: Intense flash boiling effect on spray morphology using the droplet size reduction scale

Figure 2 shows a comparison of the spray morphology of liquid ammonia using a temperature contour of droplet size reduction scale 70% and 20%. The 20% scale shows a near-spherical distribution of temperature compared to the traditional spray morphology shown in the 70% scale contour. Due to the reduced momentum and reduced droplet lifetime, the 20% droplet reduction case shows a wide and short domain where the temperature is affected by the spray, compared to narrow and deep spray region in the 70% droplet reduction case. By comparing with the schlieren image from the spray experiment [12], the corresponding spray morphology resulting from the 20% reduction does not agree with the experiment, albeit with a better agreement of vapor penetration. The weaker flash boiling case with a droplet size reduction scale of 70% is considered to be more appropriate, which gives reasonable agreement to both the spray morphology and vapor penetration.

3. Results and Discussion

3-1. Benchmark case of ammonia spray under 60 bar and 1200 K

In order to determine the combustion properties of ammonia spray without the effects from the interaction of the plumes of the seven nozzles, a benchmark case is set up based on the validated ammonia spray case with a reduction of the nozzle count to one nozzle. The simulation is conducted under engine relevant reactive conditions of 60 bar and 1200 K in air and with a reduction in volume to 0.754 L. To describe ammonia combustion, the Otomo mechanism is adopted [15]. It has been extensively validated against laminar flame speed, ignition delay, speciation from stirred reactors and NOx formation, The mechanism includes 32 species and 211 reactions.

Detailed evolution of spray temperature distribution up to 10 ms is shown in Figure 3. For an engine speed of 1000 RPM, 60-degree crank angle corresponds to 10 ms. Up to 10 ms, there is no noticeable increase in maximum temperature in the entire flow field. At the tip of the spray, where the residence time is the longest, the temperature remains around 900K. This result shows the low chemical reactivity characteristic of ammonia making it less compatible with the existing engine operation. Methods of promoting combustion in direct injection application are needed to achieve combustion.

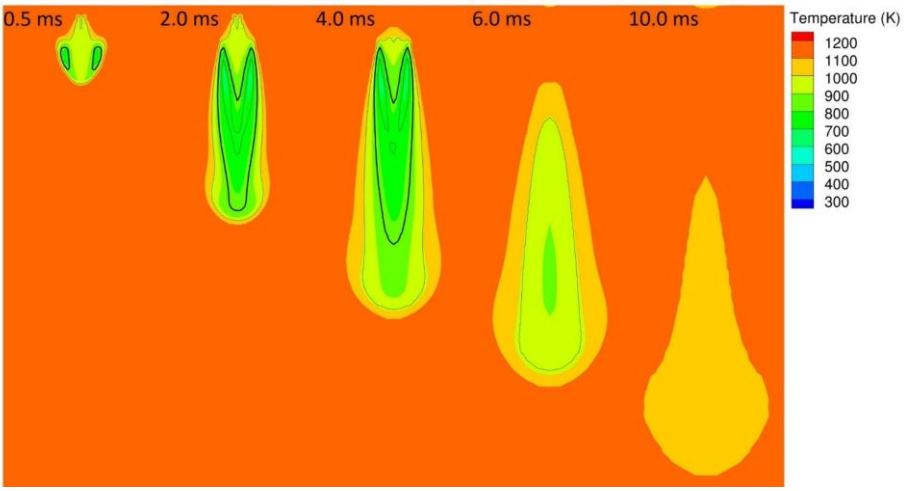

Figure 3: Evolution of the temperature (K) and equivalence ratio distribution of ammonia spray at 1200K and 60 bar. The solid lines represent iso-contours of equivalence ratio, where the stoichiometric isoline is thickened. The spacing between adjacent iso-contour is 0.5.

3-2. Effects of H_2 addition in the ambient

3.2.1 Detailed behaviors of successful ignition of ammonia spray

Dedicated exhaust gas recirculation (EGR) under fuel rich conditions is considered to promote combustion. It has been demonstrated for spark ignition engines successfully. One of the cylinders operates under fuel rich conditions, forming H_2 and other C1-C4 fragments and recirculated from to promote among the cylinders [16]. Furthermore, for ammonia combustion, H_2 can be generated *in situ* from catalytic fuel cracking [17] or thermal reforming [18]. In this work, H_2 is added into the ambient air to simulate EGR in the constant volume ammonia spray, where we define the mole fraction of H_2 in the H_2/air mixture to quantify the amount of H_2 addition. The amount of NH_3 injected stays the same for each case. We have found that even a trace amount of H_2 addition (e.g., 0.043%) is able to facilitate autoignition of ammonia spray and promotes combustion in the benchmark case shown in Fig. 3.

Figure 4 shows the evolution of total heat release rate (HRR) and the max temperature with three different concentrations of H_2 added to the air. It is seen that HRR develops two peaks, and the maximum temperature shows a two-stage rise. With decreasing H_2 addition, both heat release stages are postponed, and the maximum temperature also drops. However, the maximum temperature after the ignition (after 8 ms) shows a non-monotonic dependence on H_2 addition, with the 0.043% H_2 addition case higher than the 0.14% H_2 addition. This is most likely due to the competition between the chemical enthalpy addition from H_2 and O_2 entrainment as the composition of the ambient gas varies. For the case with 0.043% H_2 addition, higher O_2 mole fraction leads to higher flame temperature in the local non-premixed flamelets.

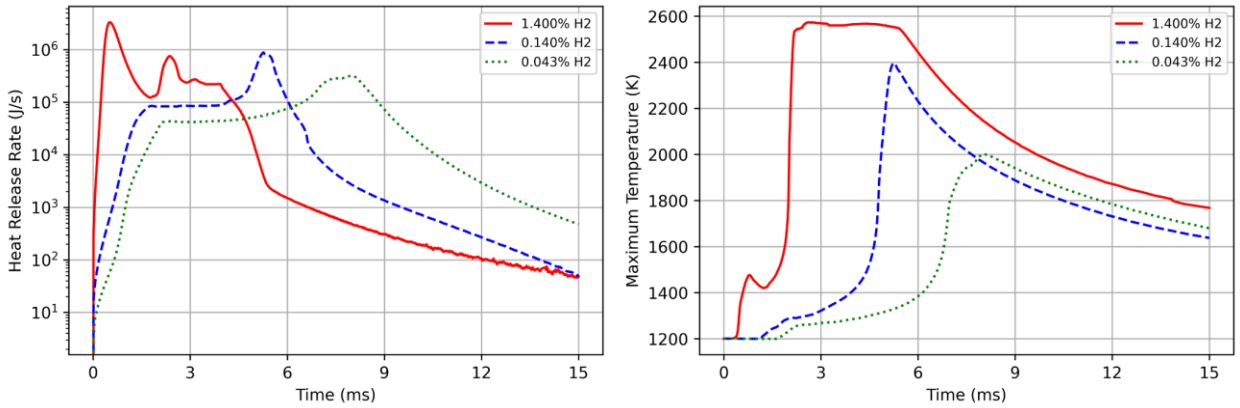

Figure 4: Total heat release rate (left), and max temperature (right) evolution for different H_2 concentrations in ambient gas.

To help understand the global results shown in Fig. 4, Figure 5 shows the temperature distribution and flow field of ammonia spray with 1.4% H_2 addition at 1200 K and 60 bars. The autoignition of H_2 in the ambient gas is shown at 0.2 ms, increasing the temperature of the chamber by approximately 123 K. Two ignition kernels on the side of the spray are formed at 2.1 ms. The flame kernel continues to grow towards the injector and the tip of the spray until a diffusion flame surrounds the entire spray. The flow field shows two eddies formed on the side of the spray at 0.1 ms, which then later grow with the spray. This behavior can explain the reason for ignition, where the recirculation of the hot gases increases the concentration of the reactive intermediate species on the sides of the spray, creating higher reactive zones compared to the surrounding areas. The recirculation zones also promote ignition at the kernels by extending the residence time.

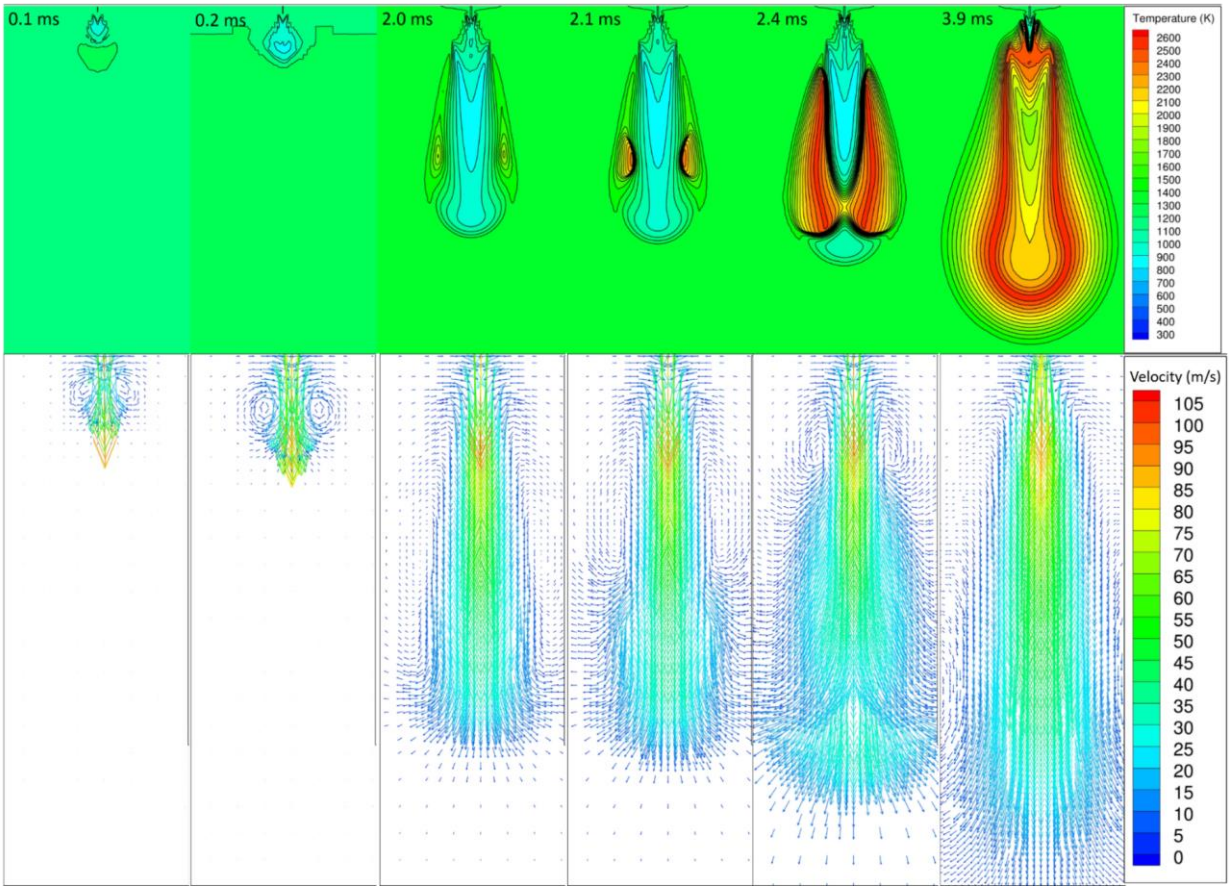

Figure 5: Evolution of temperature distribution and flow field in the case with 1.4% H_2 addition in ambient gas.

3.2.2. Thermal effects from H_2 addition.

The autoignition of H_2 in the ambient provides two effects- a thermal effect through elevating the temperature in the volume, and a chemical effect through the chemical interactions with ammonia oxidation chemistry. In order to separate the chemical effects from the thermal effects, a simulation without H_2 addition is conducted to further analyze the thermal effects at 1323 K and 65.6 bars, which corresponds to the thermodynamic conditions resulting from the autoignition of H_2. Figure 6 shows the temperature distribution of this case on the right compared to the 1.4% H_2 addition case on the left. As can be seen, the temperature of the ambient gas is identical to the elevated temperature due to H_2 autoignition, but still failed to ignite. Although the thermodynamic conditions play an important role in enhancing combustion, the chemical effects provide an irreplaceable role in promoting successful combustion of the ammonia spray. A detailed chemical analysis is needed to explore the chemical role H_2 possesses in ammonia oxidation and ignition.

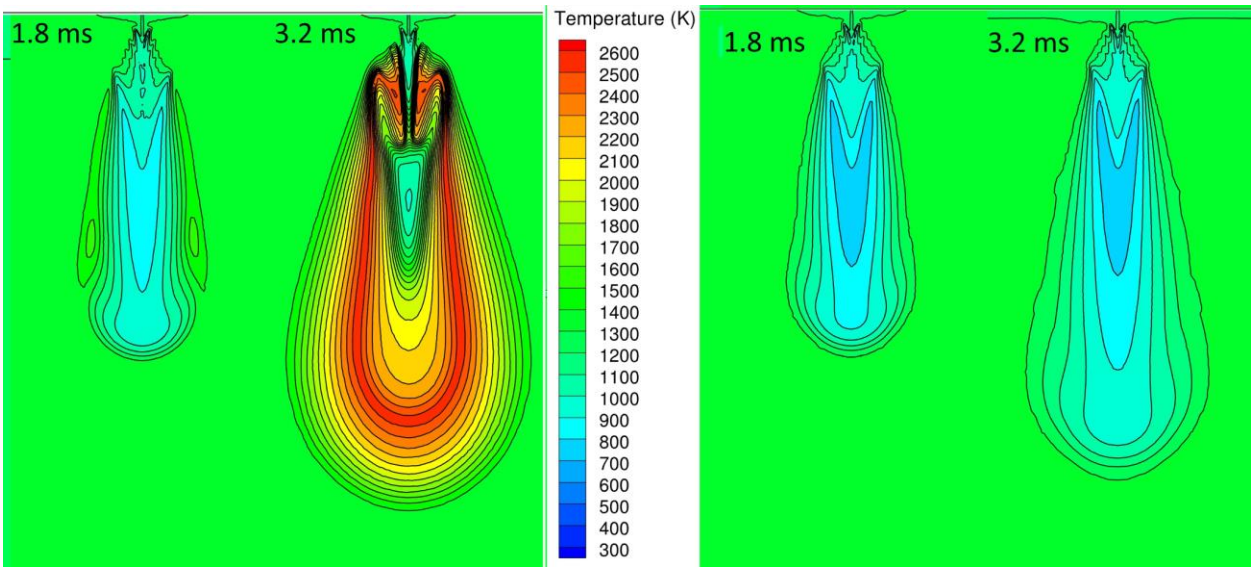

Figure 6: Temperature distribution comparison between 1.4% H_2 addition at 1200 K and 60 bar (left) and no H_2 addition at 1323K and 65.6 bar (right).

3.2.3. Chemical effects from H_2 addition

A chemical flux analysis is conducted to understand the chemical effects of H_2 addition on the ammonia spray. Mixture composition and the local thermodynamic conditions are extracted from the ignition kernel at 2.1 ms for the 1.4% H_2 addition case. CANTERA [19] is used to create a chemical flux diagram of the important species and their reactions.

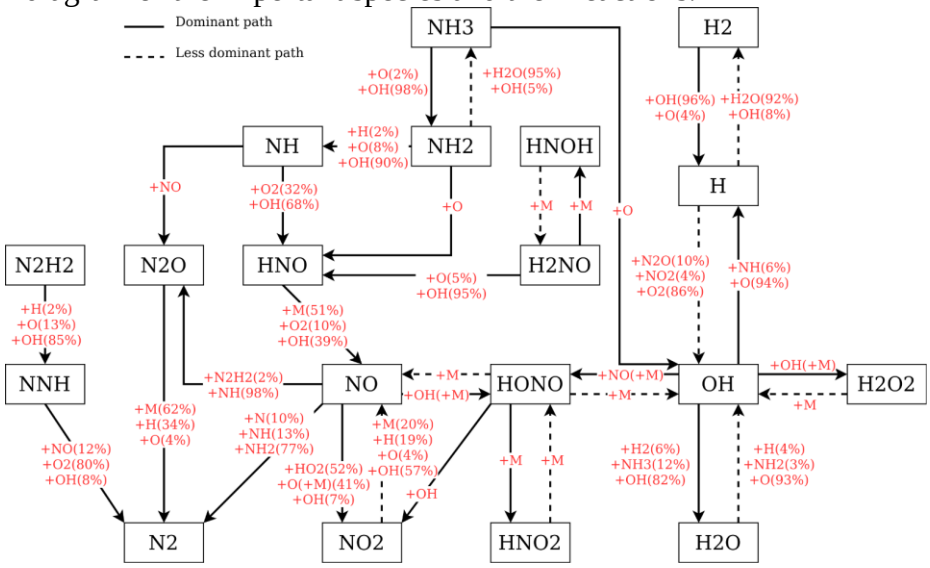

Figure 7: Chemical flux analysis at 2.1 ms inside the ignition kernel.

Figure 7 shows the chemical flux in the ignition kernel at 2.1 ms. NH_3 reacts with OH and O to form NH_2 + H_2O and NH_2 + OH, respectively. The main radical is OH which is directly formed through H_2 autoignition. 100% of NH_3 is responsible for forming NH_2, while 97.83% is responsible for forming H_2O, and 2.17% forms OH. Passed the autoignition of H_2, is is reformed through the reaction of H with H_2O and OH, then consumed by OH to create H. The main products of NH_3 are H_2O and N_2. H2O is mainly formed through the reaction of OH with OH, H_2 and NH_3, while N_2

is primarily formed from NO, N_2O and NNH. NO and NO_2 are other by-products of NH3 combustion. NO is primarily formed through the intermediate species HNO, while being consumed to form N_2O, N_2, and NO_2. On the other hand, NO_2 is formed through NO and HONO. The most useful insight from this reaction flux analysis is the enhancement of NH_3 oxidation through the radical pool from H_2 oxidation. In the practical condition where H_2 is not immediately available, local NH_3 cracking into H_2 through thermal or catalytic effects can play a dominant role for subsequent ignition process.

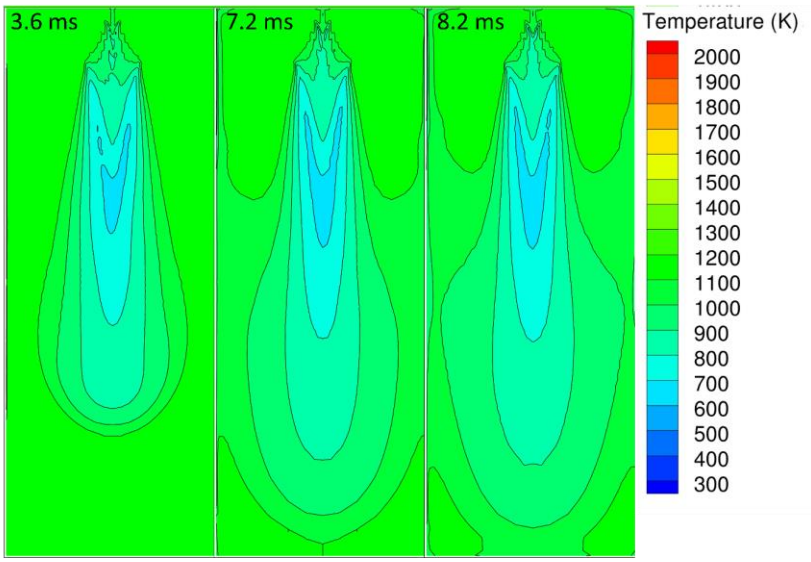

Figure 8: Temperature distribution for global equivalence ratio global equivalence ratio of 0.48 with 0.043% H_2 addition.

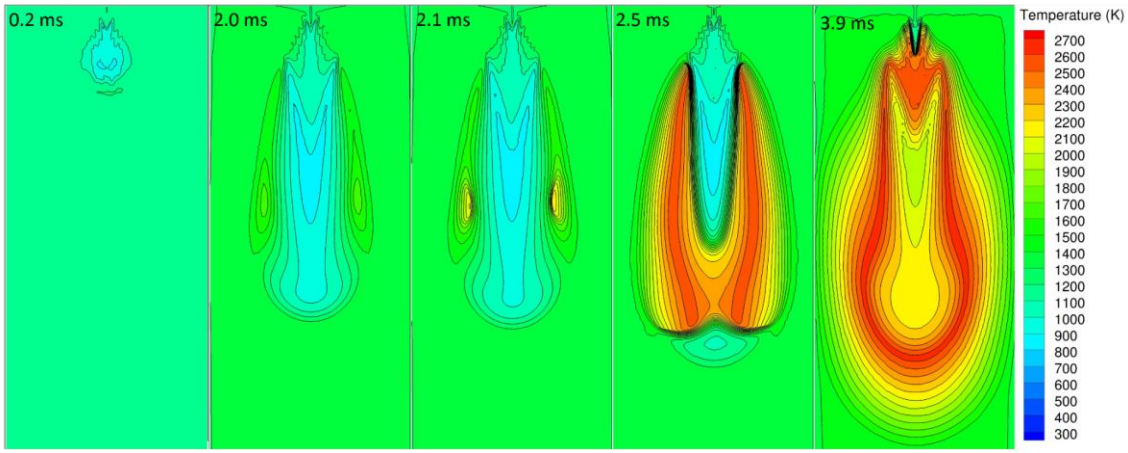

Figure 9: Evolution of temperature distribution of liquid ammonia at 0.43 global equivalence ratio with 1.4% H_2 addition to ambient gas

3-3. Charge cooling effects with increased fuel injection

In the benchmark case, the global equivalence ratio is 0.023 in order to match the injection pressure, injection time, and the chamber volume. For practical direct injection engines, a much higher global equivalence ratio is required for enhanced engine power. By maintaining the same injection pressure, we have conducted an extra simulation where the global equivalence ratio is increased to 0.48 via increasing the injection duration time to 10 ms and reducing the chamber volume to 0.087 L. Figure 8 shows a comparison of the temperature field for the cases of 0.023

(top) and 0.48 (bottom) equivalence ratios, both with 0.043% H_2 addition. Successful ignition is only observed in the leaner case. The reason is that increased amount of liquid ammonia injection has resulted in stronger charge cooling effects in the chamber, which reduces the overall gas temperature and prevents combustion.

To make combustion successful, it is expected that an increased amount of H_2 addition is needed to compensate the charge cooling effects with increased fuel injection. Figure 9 shows the evolution of temperature field with increased H_2 addition of 1.4% in the global equivalence ratio of 0.43case. Successful ignition has been achieved, where similar ignition kernels are formed in the recirculation zone of the spray with global equivalence ratio of 0.43. The detailed combustion process is largely similar to the case shown in Fig. 5. The results show that the minimum H_2 addition required to promote ignition is increased with increased liquid ammonia injection.

4. Conclusion:

The required conditions to promote ammonia spray auto-ignition are investigated through numerical simulation in this work. Simulation of ammonia spray is firstly validated against a non-reacting ammonia spray, achieving reasonable agreement with the experimental observation in the penetration distance and the spray morphology. Then the constant-volume spray simulation is extended to an engine-like condition of 60 bar and 1200 K. The results show that ammonia spray fails to achieve autoignition in the benchmark condition without the enhancement of combustion through H_2 addition to the ambient gas. It is shown that H_2 addition as low as 0.043% by volume in the ambient air leads to successful autoignition in the benchmark case. The ignition kernel is found to be in the recirculation region on the side of the spray plume. The ignition promotion benefits from the combined effects of elevated thermodynamic condition and chemical interaction from H_2 addition. The comparison then demonstrates the dominant role of chemical interaction of H_2 and ammonia oxidation chemistry, with no successful ignition due to thermal effects of H_2 addition. Reaction flux analysis shows that OH and H radicals generated by H_2 oxidation play the dominant role to initiate NH_3 oxidation, to form NH_2 and H_2, and accelerate the subsequent reactions. Charge cooling effect from the liquid ammonia is also demonstrated by increasing fuel injection. It is found that with increased fuel injection, liquid ammonia autoignition becomes more challenging and the required H_2 addition amount further increases to compensate the charge cooling effects. The numerical simulation in this study demonstrates the fundamental thermal and chemicals effects from H_2 addition in the ignition promotion of ammonia spray. The results can provide useful guidance toward the application of liquid ammonia in heavy duty direct injection engines with H_2 generated from in-situ ammonia cracking or dedicated exhaust gas recirculation.

5. Acknowledgment

PZ appreciates the support from NSF through award number 2225803.

6. References

[1] IEA, The Role of Low-Carbon Fuels in the Clean Energy Transitions of the Power Sector, IEA, Paris https://www.iea.org/reports/the-role-of-low-carbon-fuels-in-the-clean-energy-transitions-of-the-power-sector, License: CC BY 4.0, 2021.

[2] S. Ghavam, M. Vahdati, I. Wilson and P., Styring, Sustainable Ammonia Production Processes. Front. Energy Res. 9 (2021) 580808.

[3] Y. Zhao, J. Hu, L. Hua, S. Shuai, J. Wang, Ammonia storage and slip in a urea selective catalytic reduction catalyst under steady and transient conditions, Int. Eng. Chem. Res. 50 (2011) 11863–11871.

[4] A. Ichikawa, A.Hayakawa, Y. Kitagawa, A. Kunkuma, T. Kudo, and H. Kobayashi, Laminar burning velocity and Markstein length of Ammonia/hydrogen/air premixed flames at elevated pressures. Int. J. Hydrogen Energ. 40 (2015) 9570–9578.
[5] M. Comotti, S. Frigo, Hydrogen generation system for ammonia–hydrogen fuelled internal combustion engines, Int. J. Hydrogen Energ. 40 (2015) 10673-10686.
[6] K J. Richards, P.K. Senecal, E. Pomraning, CONVERGE 3.0, Convergent Science, Madison, WI (2022).
[7] M.A. Patterson, Modeling the Effects of Fuel Injection Characteristics on Diesel Combustion and Emissions," Ph.D. Thesis, University of Wisconsin-Madison, 1997.
[8] D.P. Schmidt, C. J. Rutland, A New Droplet Collision Algorithm, J. of Computational Physics 164 (2000) 62-80.
[9] A. A. Amsden, P.J. O'Rourke, T. Butler, KIVA-II: A Computer Program for Chemically Reactive Flows with Sprays, Los Alamos National Laboratory Technical Report (1989)
[10] B.E. Launder, D.B. Spalding, The numerical computation of turbulent flows, Computer Methods in Applied Mechanics and Engineering, 3 (1974) 269-289.
[11] P.K. Senecal, E. Pomraning, K.J. Richards, Multi-Dimensional Modeling of Direct- Injection Diesel Spray Liquid Length and Flame Lift-off Length using CFD and Parallel Detailed Chemistry, SAE Paper (2003).
[12] R. Pelé, C. Mounaïm-Rousselle, P. Bréquigny, C. Hespel, J. Bellettre, First Study on Ammonia Spray Characteristics with a Current GDI Engine Injector. Fuels 2(2021) 253–271.
[13] M. Xu, Y. Zhang, W. Zeng, G. Zhang, M. Zhang, Flash Boiling: Easy and Better Way to Generate Ideal Sprays than the High Injection Pressure, SAE Int. J. of Fuels and Lubricants 6 (2013) 137-148.
[14] C. Price, A. Hamzehloo, P. Aleiferis, R. Richardson, An Approach to Modeling Flash-Boiling Fuel Sprays for Direct-Injection Spark-Ignition Engines, Atomization and Sprays, 26(2016) 1197-1239.
[15] J. Otomo, M. Koshi, T. Mitsumori, H. Iwasaki, K. Yamada, Chemical kinetic modeling of ammonia oxidation with improved reaction mechanism for ammonia/air and ammonia/hydrogen/air combustion, Int. J. of Hydrogen Energy 43 (2018) 3004-3014.
[16] T. Alger, B. Mangold, Dedicated EGR: A New Concept in High Efficiency Engines, SAE Int. J. Engines 2 (2009) 620-631.
[17] Y. Kojima, High purity hydrogen generation from ammonia. ACS Washington Meeting (2017).
[18] W. Wang, J. Herreros, A. Tsolakis, A. York, Ammonia as hydrogen carrier for transportation; investigation of the ammonia exhaust gas fuel reforming, Int. J. of Hydrogen Energy 38 (2013) 9907-9917.
[19] D.G. Goodwin, H.K. Moffat, I. Schoegl, R.L. Speth, and B. Weber, Cantera: An object-oriented software toolkit for chemical kinetics, thermodynamics, and transport processes. https://www.cantera.org.